PHYSICAL REVIEW D **86,** 084033 (2012)

Simulations of unequal-mass black hole binaries with spectral methods

Luisa T. Buchman,[1] Harald P. Pfeiffer,[2] Mark A. Scheel,[1] and Béla Szilágyi[1]

[1]*Theoretical Astrophysics 350-17, California Institute of Technology, Pasadena, California 91125, USA*

[2]*Canadian Institute for Theoretical Astrophysics, University of Toronto, Toronto, Ontario M5S 3H8, Canada*

(Received 14 June 2012; published 12 October 2012)

This paper presents techniques and results for simulations of unequal-mass, nonspinning binary black holes with pseudospectral methods. Specifically, we develop an efficient root-finding procedure to ensure the black hole initial data have the desired masses and spins; we extend the dual coordinate frame method and eccentricity removal to asymmetric binaries. Furthermore, we describe techniques to simulate mergers of unequal-mass black holes. The second part of the paper presents numerical simulations of nonspinning binary black holes with mass ratios 2, 3, 4, and 6, covering between 15 and 22 orbits, merger and ringdown. We discuss the accuracy of these simulations, the evolution of the (initially zero) black hole spins, and the remnant black hole properties.

DOI: 10.1103/PhysRevD.86.084033 PACS numbers: 04.25.D−, 02.70.Hm, 04.25.dg, 04.30.−w

I. INTRODUCTION

Numerical simulations of the inspiral and coalescence of two black holes [1] are an important tool for exploiting upcoming gravitational wave detectors such as Advanced LIGO, VIRGO, and LCGT/KAGRA [2–6]. Increasingly larger sets of simulations have begun to explore the parameter space of binary black holes (BBHs), most notably through the NINJA [7–9] and NRAR [10] collaborations.

One important subset of this parameter space comprises nonspinning BBHs. Head-on collisions have been studied first [11,12], followed by simulations of inspiral and coalescence of binaries that start in a quasicircular orbit. One well-studied phenomenon is the kick imparted to the remnant black hole as a result of the collision of unequal-mass black holes [13,14]; the form of this kick as a function of the initial black hole masses is constrained by symmetry considerations [15]. Numerical simulations of nonspinning BBH systems also formed the basis of analytic waveform models and applications to gravitational wave data analysis [16–22], tuning of effective-one-body waveform models [23–26], multipolar analysis [27,28], and investigations into the periastron advance of binary black holes [29,30]. Recently, the range of mass ratios covered by unequal-mass binaries has been extended to mass ratios 10:1 [31] and up to 100:1 [32–34].

Numerical simulations are still too computationally expensive to include enough binary orbits for data analysis. Therefore, simulations are matched to post-Newtonian inspirals to obtain ''hybrid'' waveforms of sufficient length. This matching must be done early enough in the inspiral so that the post-Newtonian expressions are still accurate. During the last year, it has become increasingly apparent that current numerical simulations are still not long enough to provide an accurate match: the frequency range where post-Newtonian and numerical waveforms are matched with each other is currently so high that neglected higher-order terms in even state-of-the-art post-Newtonian models lead to a noticeable impact on data analysis [19,35–40].

Unfortunately, the computational expense of a BBH inspiral is a steep function of its initial frequency. For instance, at lowest post-Newtonian order [41], a BBH inspiral starting at an initial frequency Ω_i merges at a time

$$T = \frac{5}{256}\,\eta^{-1}(M\Omega_i)^{-8/3}M, \tag{1}$$

where M is the total mass of the binary and η its symmetric mass ratio $\eta = M_1M_2/(M_1 + M_2)^2$. So even if the computational expense were proportional to the evolution time T, it would be expensive to significantly reduce Ω_i; in practice, the situation is even worse because the computational expense (for a given accuracy) increases superlinearly with T. Therefore, long numerical inspiral simulations (lasting $\gtrsim 10$ orbits) are rare, and are generally available only for equal-mass binaries without spin [42], or with equal spin magnitudes parallel to the orbital angular momentum [43,44].

This paper revisits simulations of nonspinning unequal-mass binary black holes, and describes accurate many-orbit waveforms, including subdominant (ℓ, m) modes. Our simulations are performed with the Spectral Einstein Code (SpEC) [45], a multidomain pseudospectral evolution code. There are several motivations for this work. First, we present an efficient technique to perform 10-dimensional root-finding which is necessary to construct BBH initial data with specified masses and spins. Second, we present algorithms for simulations of unequal-mass BBH systems with spectral methods. Third, we present and carefully discuss a series of long duration, high-accuracy, unequal-mass nonspinning BBH simulations, lasting between 15 and 22 orbits. These simulations extend the parameter space covered by spectral BBH evolutions, and improve in length and accuracy already existing simulations which use alternative numerical techniques. The simulations presented here also provide additional data points

for remnant masses, spins, and kick velocities, which we compare with already published calculations and analytical models. Finally, we provide a study of tidal spin-up of initially nonspinning black holes.

This paper is organized as follows. Section II presents details of our numerical implementation. First, the quasicircular, quasiequilibrium initial data [46,47] require root finding to adjust free parameters so that after the initial data construction, the black holes have specified masses and approximately zero spins—we introduce an efficient algorithm for performing this root finding. Second, we extend the dual-frame approach [48] to unequal-mass binaries, and discuss how we choose orbital parameters that result in inspirals of orbital eccentricity $e < 10^{-4}$. Finally, we describe the handling of merger and ringdown, improving on previous treatments [42,43,49] of black hole mergers performed with spectral multidomain methods. Section III presents numerical results for mass ratios 2, 3, 4, and 6. These include results of convergence tests, discussion of the black hole spin, detailed analysis of the leading higher-order modes of the emitted gravitational waveform, and discussion of the properties of the remnant black hole: mass, spin, and recoil velocity. Section IV summarizes and discusses our main results.

We note that the simulations presented here have already been used in the following published work: fitting effective-one-body models [25,26] and measuring the periastron advance for BBHs [29]. They have also been contributed to the Ninja2 [9] and NRAR projects [10]. Further, the formalism for setting initial data (cf. Sec. II B) and for eccentricity removal (cf. Sec. II D) was employed in Refs. [30,50].

II. FORMALISM AND NUMERICAL METHODS

A. Overview

Our goal is to compute the last ~20 inspiral orbits, merger, and ringdown of binary black holes with mass ratio $q = M_1/M_2 \geq 1$, negligible spins of the black holes, and vanishingly small orbital eccentricity. This requires a rather complex sequence of steps:

(1) Choose the physical black hole masses M_1, M_2.
(2) Decide on the initial coordinate separation D_0, and choose tentative values for the orbital frequency Ω_0 and its time derivative, parameterized by $\dot{a}_0 = \dot{D}(t)/D_0$ (for instance, based on post-Newtonian formulae).
(3) Fine-tune the 10 parameters that enter the initial data so that the initial data contain black holes with desired masses, desired spins (here, zero), and vanishing center-of-mass motion.
(4) Perform a short evolution lasting 2–3 orbits of the resulting initial-data set.
(5) From the evolution in step 4, extract information about the orbit of the binary, and estimate the orbital eccentricity e. If e is unacceptably large, correct Ω_0 and $\dot{a}_0$, and go back to step 3.
(6) If the orbital eccentricity e is sufficiently small, continue the evolution through the remaining inspiral (for the current paper, we require $e < 10^{-4}$).
(7) Simulate plunge, merger, and ringdown.

In order to accomplish our goal, we needed to make several refinements to previous procedures used in SpEC for equal-mass [42,43,51,52] and more generic (including $q = 2$ unequal-mass) [49] BBH simulations. These are that step 3 was not necessary in previous evolutions of simpler configurations, and is explained in detail in Sec. II B below. Modifications to the inspiral evolutions in step 4 are detailed in Sec. II C. Eccentricity removal in step 5 is generalized to mass ratios $q \neq 1$ in Sec. II D. Improvements to the merger and ringdown phases (step 7) are described in Sec. II E. Finally, Sec. II F summarizes code infrastructure that has not changed since earlier simulations; examples are apparent horizon finders and wave extraction.

B. Initial data

Quasiequilibrium binary black hole initial data [46,47,53] are constructed with the conformal thin sandwich method [54,55]. This formalism results in a set of five coupled nonlinear elliptic equations, which are solved numerically with a multidomain pseudospectral collocation method [56].

As in earlier work, we employ the simplifying assumptions of conformal flatness and maximal slicing. Thirteen further real parameters uniquely determine the complete initial data set. The orbital characteristics are determined by the three parameters D_0 (coordinate separation), Ω_0 (orbital frequency), and $\dot{a}_0$ (radial expansion factor); their choice will be discussed in detail in Sec. II D. The remaining 10 parameters

$$\underline{u} = (r_1, r_2, \vec{\Omega}_1, \vec{\Omega}_2, X, Y) \tag{2}$$

are the radii r_1, r_2 of the excision spheres, the angular velocities of the horizons, $\vec{\Omega}_1$, $\vec{\Omega}_2$, and the coordinate centers of the excision spheres, parameterized by X and Y via $\vec{c}_1 = (X, Y, 0)$ and $\vec{c}_2 = (X - D_0, Y, 0)$. We assume that the black holes start in the xy plane, with orbital angular frequency parallel to the z axis, i.e., the vectorial orbital frequency is written as $\vec{\Omega}_0 = (0, 0, \Omega_0)$.

The physical parameters (masses, spins, linear momentum) can only be computed *after* the constraint equations are solved, whereas the initial data parameters $\underline{u}$ must be chosen beforehand. Therefore, 10-dimensional root finding is required, to satisfy

$$\underline{F}(\underline{u}) \equiv (M_1 - M_1', M_2 - M_2', \vec{\chi} - \vec{\chi}_1', \vec{\chi} - \vec{\chi}_2', P^x_{\mathrm{ADM}}, P^y_{\mathrm{ADM}}) = 0. \tag{3}$$

Here, $M_{1,2}$, $\vec{\chi}_{1,2}$, and $\vec{P}_{\mathrm{ADM}}$ are, respectively, the masses, dimensionless spins, and total linear momentum,

determined from the solution of the constraint equations, whereas $M'_{1,2}$ and $\vec{\chi}'_{1,2}$ are the desired masses and dimensionless spins of the black holes. We also demand that the initial Arnowitt-Deser-Misner (ADM) linear momentum $\vec{P}_{\rm ADM}$ vanish. The x and y components of $\vec{P}_{\rm ADM}$ are controlled by the choice of Y and X, respectively. Its z component $P^z_{\rm ADM}$ vanishes by symmetry $z \to -z$ (in generic spinning cases, this will no longer be the case).

In this paper, we will evolve only nonspinning black holes such that $\vec{\chi}'_{1,2} = 0$, but we present the root finding for generic spins.

Each function evaluation $\underline{F}(\underline{u})$ requires solving the elliptic constraint equations. At high resolutions, this requires a few hours of wall-clock time. Because root finding with standard techniques such as the Newton-Raphson method [57] requires many function evaluations to compute the Jacobian, this would result in inconveniently long run times.[1] To reduce computational expense, we replace the exact Jacobian $\partial \underline{F}/\partial \underline{u}$ by an *approximation* $\mathcal{J}_A$ and perform a Newton-Raphson iteration employing $\mathcal{J}_A$. That is, given parameters $\underline{u}^{(k)}$, improved parameters are determined by

$$\Delta \underline{u} \equiv \underline{u}^{(k+1)} - \underline{u}^{(k)} = -\mathcal{J}_A^{-1} \underline{F}(\underline{u}^{(k)}), \tag{4}$$

where $\mathcal{J}_A$ is evaluated at $\underline{u}^{(k)}$.

Efficiency of this technique hinges crucially on the quality of the approximated Jacobian $\mathcal{J}_A$. We compute $\mathcal{J}_A$ based on considerations that are valid for single black hole initial data, and/or Newtonian gravity. Specifically, for conformally flat single black hole initial data with maximal slicing, the mass is proportional to the radius of the excision sphere; therefore, we take

$$\frac{\partial M_A}{\partial r_A} = \frac{M_A}{r_A}, \qquad A = 1, 2. \tag{5a}$$

Furthermore, for Kerr black holes with small spin, the dimensionless spin parameter $\vec{\chi}$ is related to the angular frequency of the horizon $\vec{\Omega}_H$ by $\vec{\chi} = 4M\vec{\Omega}_H$, where M is the mass of the Kerr black hole. For BBHs, the horizon frequency $\vec{\Omega}_A$ measures spin in *addition* to corotation, so that $\vec{\chi}_A = 4M_A(\vec{\Omega}_A - \vec{\Omega}_0)$, from which follows

$$\frac{\partial \vec{\chi}_A}{\partial r_A} = \frac{\vec{\chi}_A}{r_A}, \qquad \frac{\partial \vec{\chi}_A}{\partial \vec{\Omega}_A} = 4M_A, \qquad A = 1, 2. \tag{5b}$$

[1] In earlier work on equal-mass binaries with equal aligned spins, this root finding was not performed. For those configurations, symmetry implies $r_1 = r_2$, $\vec{\Omega}_1 = \vec{\Omega}_2$ and $X = Y = 0$. The radii $r_1 = r_2$ were chosen to be some fixed value, and the final black hole masses were simply measured (rather than controlled). For the nonspinning simulation [52], $\vec{\Omega}_{1,2}$ were fixed at their values from quasicircular nonspinning initial data [46]; for the spinning simulation [43], $\vec{\Omega}_1 = \vec{\Omega}_2$ was chosen parallel to the z axis, and the resulting black hole spin was just measured (rather than controlled).

Finally, in Newtonian gravity, the linear momentum is given by $\vec{P} = M_1\vec{\Omega}_0 \times \vec{c}_1 + M_2\vec{\Omega}_0 \times \vec{c}_2$. Substituting in $\vec{\Omega}_0 = (0, 0, \Omega_0)$, $\vec{c}_1 = (X, Y, 0)$, $\vec{c}_2 = (X - D_0, Y, 0)$, one finds

$$\frac{\partial P^x}{\partial r_1} = -\frac{M_1}{r_1}\Omega_0 Y, \qquad \frac{\partial P^x}{\partial r_2} = -\frac{M_2}{r_2}\Omega_0 Y, \tag{5c}$$

$$\frac{\partial P^x}{\partial Y} = -(M_1 + M_2)\Omega_0, \tag{5d}$$

$$\frac{\partial P^y}{\partial r_1} = \frac{M_1}{r_1}\Omega_0 X, \qquad \frac{\partial P^y}{\partial r_2} = \frac{M_2}{r_2}\Omega_0 (X - D_0), \tag{5e}$$

$$\frac{\partial P^y}{\partial X} = (M_1 + M_2)\Omega_0. \tag{5f}$$

Equations (5a)–(5f) are the only nonzero components of $\mathcal{J}_A$. Because the Jacobian is so sparse, it is trivial to solve Eq. (4), and one obtains

$$\Delta r_A = -r_A \frac{M_A - M'_A}{M_A}, \qquad A = 1, 2, \tag{6a}$$

$$\Delta\vec{\Omega}_A = -\frac{\vec{\chi}_A - \vec{\chi}'_A}{4M_A} + \frac{M_A - M'_A}{4M_A^2}\vec{\chi}_A, \qquad A = 1, 2, \tag{6b}$$

$$\Delta X = \frac{-P^y_{\rm ADM}}{(M_1 + M_2)\Omega_0} + \frac{X(M_1 - M'_1) + (X - D_0)(M_2 - M'_2)}{M_1 + M_2}, \tag{6c}$$

$$\Delta Y = \frac{P^x_{\rm ADM}}{(M_1 + M_2)\Omega_0} + \frac{Y(M_1 - M'_1 + M_2 - M'_2)}{M_1 + M_2} \tag{6d}$$

In these equations, primed quantities are the desired values, whereas unprimed quantities are determined from the initial data computed from parameters $\underline{u}^{(k)}$.

Figure 1 demonstrates the efficiency of this procedure for two configurations. During the first iterations of root finding, we solve the constraint equations only to lowest resolution. We begin to increase the resolution $k_{\rm Ell}$ of the elliptic solver when the residual $|\underline{F}|$ falls within a factor of 10^4 of our target tolerance 10^{-7}. Because solving the constraint equations at low resolution is very quick, the overall cost of the root finding is dominated entirely by the solutions of the constraint equations at highest resolution, and thus, the entire root finding adds only a small amount of wall-clock time.

As is apparent in Fig. 1, the quadratic convergence of Newton-Raphson algorithm is lost because of the approximations entering $\mathcal{J}_A$. We find roughly linear convergence where each iteration reduces the error by a certain factor. The convergence rate depends on how closely $\mathcal{J}_A$ resembles the exact Jacobian. Convergence is not exactly linear, because we delay increasing the resolution of the elliptic solver until as high k as possible, to gain maximum speed up from the lower resolution solutions.

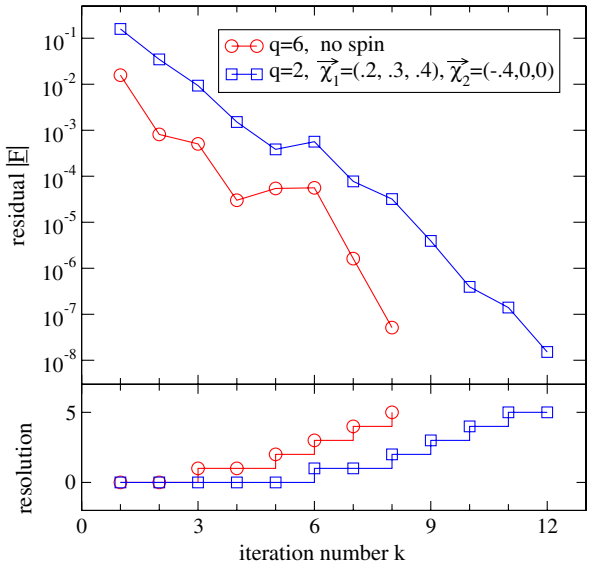

FIG. 1 (color online). Residual $|\underline{F}|$ of the initial-data root-finding procedure (top panel) vs iteration number. The lower panel indicates the numerical resolution of each elliptic constraint solve, with 5 being highest resolution (each increase of this integer corresponds to adding a certain number of basis functions, cf. Fig. 6 of Ref. [47]).

C. Evolution of inspiral phase

The Einstein evolution equations are solved with the pseudospectral evolution module of SpEC, as described in Ref. [42]. This code evolves a first-order representation [58] of the generalized harmonic system [59–61] and includes terms that damp away small constraint violations [58,61,62]. The computational domain extends from excision boundaries located just inside each apparent horizon to some large radius, and is divided into subdomains with simple shapes (e.g., spherical shells, cubes, cylinders). No boundary conditions are needed or imposed at the excision boundaries, because all characteristic fields of the system are outgoing (into the black hole) there. The boundary conditions on the outer boundary [58,63,64] are designed to prevent the influx of unphysical constraint violations [65–71] and undesired incoming gravitational radiation [72,73], while allowing the outgoing gravitational radiation to pass freely through the boundary. Interdomain boundary conditions are enforced with a penalty method [74,75].

The gauge freedom in the generalized harmonic formulation of Einstein's equations is fixed via a freely specifiable gauge source function H_a that satisfies the constraint

$$0 = C_a \equiv \Gamma_{ab}{}^{b} + H_a, \tag{7}$$

where $\Gamma^{a}{}_{bc}$ are the spacetime Christoffel symbols. During the inspiral, we choose H_a as in Refs. [42,43,52].

In order to treat moving holes using a fixed grid, we employ multiple coordinate frames [48]: the equations are solved in an "inertial frame" which is asymptotically Minkowski, but the grid is fixed in a "grid frame" in which the black holes do not move. The motion of the holes is accounted for by dynamically adjusting the coordinate mapping between the two frames.[2] This coordinate mapping differs from our earlier work, and is described below in Sec. II C 1. Furthermore, the choice of constraint damping parameters is important for stability, and it is discussed in Sec. II C 2.

1. Dual Frames and Control System

SpEC utilizes two coordinate systems [48]: grid coordinates x^i, in which the domain decomposition is fixed, and inertial coordinates $x^{\bar{i}}$, in which the black holes orbit around each other. The mapping between these coordinate systems is chosen such that in grid coordinates, the black holes remain centered on the excision spheres. In earlier simulations of equal-mass binaries [48,51,52], this map was chosen to be a rotation and an overall scaling. Unequal-mass binaries will acquire a kick in the orbital plane; therefore, we add a translation to the mapping between inertial and grid coordinates:

$$x^{\bar{i}} = a(t) R^{\bar{i}}{}_{i} x^i + T^{\bar{i}}. \tag{8}$$

Here, $a(t)$ is the overall scale factor, $T^{\bar{i}} = (T^{\bar{x}}, T^{\bar{y}}, 0)$ represents the translation, and

$$R^{\bar{i}}{}_{i} = \begin{pmatrix} \mathbf{R}_{\phi} & \mathbf{0} \\ \mathbf{0} & 1 \end{pmatrix}, \quad \mathbf{R}_{\phi} = \begin{pmatrix} \cos\phi & -\sin\phi \\ \sin\phi & \cos\phi \end{pmatrix} \tag{9}$$

is the rotation matrix for a rotation by the angle $\phi(t)$ about the z axis. The rotation and translation act only on the x and y coordinates, because a nonspinning unequal-mass binary is, by symmetry, confined to remain in the xy plane.[3] Equation (8) is combined with an additional radial coordinate transformation that stretches the region far from the black holes such that the outer boundary moves very slowly inward. The motion of the outer boundary is nonzero so that zero speed modes are outgoing and do not require a boundary condition, but small enough that the outer boundary moves inward only a few M during the entire simulation.

The mapping Eq. (8) is determined by four free functions, $\lambda_\alpha \equiv \{a(t), \phi(t), T^{\bar{x}}(t), T^{\bar{y}}(t)\}$ (where α labels the four functions). The functions $\lambda_\alpha(t)$ must be chosen dynamically such that the black hole horizons remain centered on the excision boundaries. As described in Ref. [48], this is accomplished through a control system

[2]All coordinate quantities (e.g., trajectories, waveform extraction radii) in this paper are given with respect to the inertial frame unless noted otherwise.

[3]Spinning, unequal-mass binaries with both black hole spins *parallel* to the orbital angular momentum will also remain in a fixed orbital plane. Our discussion applies equally well to these systems.

which constantly monitors the location of the black holes, and dynamically changes the functions $\lambda_\alpha(t)$ appropriately. Such a control system is formulated most easily in terms of control parameters $Q_\alpha \equiv \{Q_a, Q_\phi, Q_x, Q_y\}$ which have the properties (i) that $Q_\alpha = 0$ when the black holes are at their desired locations, and (ii) for small values of Q_α, changing the mapping parameters λ_α changes the control parameters Q_α according to

$$\frac{\partial Q_\alpha}{\partial \lambda_\beta} = -\delta^\alpha{}_\beta, \quad \text{for } |Q_\alpha| \ll 1. \tag{10}$$

The control parameters must be given in terms of the moving coordinates of the centers of the apparent horizons, $c^i_{1,2}$, and they must vanish when $c^i_{1,2}$ are at the desired locations, namely, when they are at their values in the initial data $(c^i_{1,2})_{t=0}$. The derivatives in Eq. (10) are to be taken at constant inertial coordinates of the centers of the horizons.

To begin, we define

$$(\Delta_x(t), \Delta_y(t), \Delta_z(t)) \equiv \vec{c}_1(t) - \vec{c}_2(t), \tag{11}$$

$$D(t) \equiv [\Delta^2_x(t) + \Delta^2_y(t)]^{1/2}. \tag{12}$$

Because of symmetries, Δ_z is always zero, and will not be used. The control parameters for the expansion factor $a(t)$ and the rotation angle $\phi(t)$ are given by

$$Q_a = a(t)\left(\frac{D(t)}{D_0} - 1\right), \tag{13a}$$

$$Q_\phi = \frac{\Delta_y(t)}{D(t)}. \tag{13b}$$

It is straightforward to verify that Q_a and Q_ϕ satisfy Eq. (10). The control parameters for the translation are somewhat more involved. We use the ansatz

$$\begin{pmatrix} Q_x \\ Q_y \end{pmatrix} = a(t)\mathbf{R}_{\phi(t)}\left[\begin{pmatrix} x_B \\ y_B \end{pmatrix} + \mathbf{M}\begin{pmatrix} \Delta_x \\ \Delta_y \end{pmatrix}\right], \tag{13c}$$

where $\mathbf{M}$ is a constant 2×2 matrix, and we demand that $\mathbf{M}$ commutes with $\mathbf{R}_{\phi(t)}$. Because $\mathbf{M}$ and $\mathbf{R}_{\phi(t)}$ commute, Eq. (13c) can be rewritten in inertial coordinates as

$$\begin{pmatrix} Q_x \\ Q_y \end{pmatrix} = \begin{pmatrix} \bar{x}_B \\ \bar{y}_B \end{pmatrix} + \mathbf{M}\begin{pmatrix} \bar{\Delta}_x \\ \bar{\Delta}_y \end{pmatrix} - \begin{pmatrix} T^{\bar{x}} \\ T^{\bar{y}} \end{pmatrix}, \tag{14}$$

which makes it obvious that Q_x and Q_y satisfy Eq. (10).

To close this discussion, we must compute the matrix $\mathbf{M}$. The requirements that $\mathbf{M}$ commute with $\mathbf{R}_\phi$ and that $Q_x = Q_y = 0$ for $c^i_{1,2} = (c^i_{1,2})_{t=0}$ determine $\mathbf{M}$ uniquely:

$$\mathbf{M} = \frac{1}{D_0}\begin{pmatrix} x_{A,0} & -y_{A,0} \\ y_{A,0} & x_{A,0} \end{pmatrix}. \tag{15}$$

The mapping given in Eq. (8) and the control parameters, given in Eq. (13), are then combined with the feedback control system described in Ref. [48] in order to evolve the unequal-mass BBH through the inspiral phase.

2. Constraint Damping

In order to suppress violations of the generalized harmonic gauge constraint Eq. (7) (cf. Refs. [62,76]), and of the auxiliary constraints that arise from the reduction of the generalized harmonic evolution system to first order form (cf. Refs. [58,77]), we introduce so-called *constraint damping terms* in the generalized harmonic evolution equations (see Ref. [58]). These terms are proportional to the *constraint damping parameters* γ_0 and γ_2.

Simulations with mass ratios $q = \{2, 3\}$ were found to be stable with the same constraint damping parameters as those used in Ref. [52]. However, for the higher mass ratios $q = \{4, 6\}$, we encountered constraint violations which grew exponentially on time scales of several $100M$. We found that toward the outer edges of the cylindrical subdomains, the constraint damping parameters must be sufficiently large in order to suppress exponential constraint growth. In the overlap between the inner spherical shells and the cylinders, an instability develops unless the constraint damping is sufficiently *small*. Furthermore, we were not able to achieve stable evolutions with $\gamma_0 = \gamma_2$. After considerable experimentation, we settled on a sum of Gaussians:

$$M\gamma_0 = 8e^{-(r_1/1.3M)^2} + 16e^{-(r_2/M)^2} + f_{\text{far-field}}(r), \tag{16}$$

$$M\gamma_2 = 8e^{-(r_1/1.3M)^2} + 40e^{-(r_2/M)^2} + f_{\text{far-field}}(r) \tag{17}$$

with far-field terms $f_{\text{far-field}} = 0.2e^{-(r/60M)^2} + 0.001$. Here, r_1 and r_2 are the coordinate distances from the centers of each hole, and r is the distance from the origin. The choices Eqs. (16) and (17) were found to work well even for $q = \{2, 3\}$, and all simulations presented here use them.

We infer from these results that the domain decomposition with spheres overlapping cylinders is not always stable, and that stability depends sensitively on certain geometric details. Recent shorter simulations that do not have overlapping subdomains do not show such sensitivity. However, the domain decomposition of spheres and cylinders is computationally more efficient, and therefore we employ it during long inspiral simulations.

D. Eccentricity removal

The procedure for eccentricity removal developed in Refs. [51,52] assumed an equal-mass binary. Generalization to unequal-mass binaries is straightforward. As in Ref. [52], we fit the radial velocity (represented by the time derivative of the proper separation $s(t)$ between the horizons) by the functional form

$$\frac{ds}{dt} = v_{\text{insp}}(t) + B\cos(\omega t + \phi). \tag{18}$$

Here, $v_{\rm insp}(t)$ is a monotonic function varying on the (long) inspiral time scale; this function captures the desired zero-eccentricity inspiral driven by radiation reaction. We take here the functional form

$$v_{\rm insp}(t) = v_0 + v_1 t + v_2 t^2, \tag{19}$$

with three fitting parameters v_0, v_1, v_2. However, in more recent work [50], we describe fitting functions that result in more robust behavior. The oscillating piece $B\cos(\omega t + \phi)$ captures superposed oscillation due to nonzero orbital eccentricity—the goal is to reduce the amplitude of this piece.

For unequal masses, the black holes have different separations from the origin, and therefore have different radial velocities. To avoid dealing with each black hole independently, we consider the initial data specified in terms of a Hubble-like radial expansion factor $\dot{a}_0$, which induces radial velocities proportional to the distance to the origin, $v_r^i = \dot{a}_0 x^i$ at a coordinate location x^i. The updating formulas become

$$\Omega_{0\,\rm new} = \Omega_0 + \frac{B}{2s_0}\sin(\phi), \tag{20}$$

$$\dot{a}_{0\,\rm new} = \dot{a}_0 - \frac{B}{s_0}\cos(\phi). \tag{21}$$

The orbital eccentricity is given by

$$e_{ds/dt} = \frac{B}{s_0\omega}, \tag{22}$$

which is the same formula as for the equal-mass case.

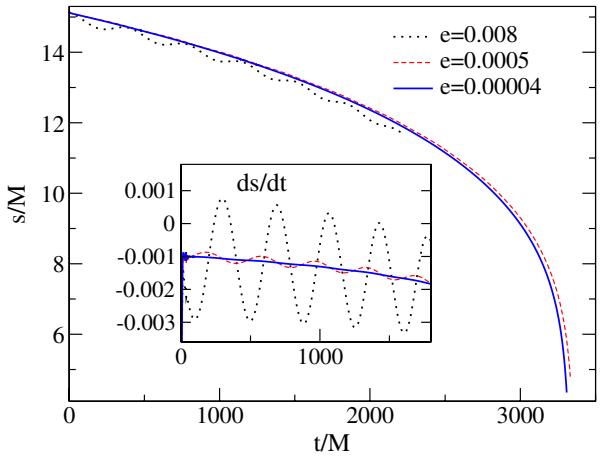

FIG. 2 (color online). Eccentricity removal for mass ratio $q = 4$. The main panel shows proper separation as a function of time, the inset radial velocity ds/dt. Initial data parameters based on TaylorT3 post-Newtonian approximation result in the black dotted line with $e \approx 0.008$. The red dashed and the solid blue lines represent two iterations of eccentricity removal, for a final eccentricity of $e \approx 4 \times 10^{-5}$.

Overall, eccentricity removal works as well here as for the equal-mass cases considered previously. Figure 2 shows that with each iteration, e drops by about a factor of 10. The most important factor for effective eccentricity removal is the quality of the fit. The fitting interval $[t_1, t_2]$ can start only after transients due to junk radiation have decayed. However, because the fit is used to infer radial velocity and acceleration at time $t = 0$, the fitting interval needs to be sufficiently early in the run to allow accurate extrapolation from the fitting interval back to $t = 0$. Finally, the fitting interval needs to be long enough to allow a reliable fit of the frequency ω, i.e., it needs to be longer than one period of the radial oscillations. Inclusion of the term quadratic in t in Eq. (19) significantly improves the quality of the fits and the effectiveness of the eccentricity removal. For the runs described here, we choose t_1 on the order of $100M$ and t_2 on the order of $1000M$.

E. Evolution of merger and ringdown

The evolution algorithm for the inspiral described in Sec. II C fails when the black holes approach each other too closely. This failure is caused by several factors. First, the gauge fields H_a are chosen during inspiral to be time-independent in the grid frame. This works well for the inspiral because the solution (in the grid frame) is roughly time-independent near the black holes. Near merger, however, this gauge leads to the formation of coordinate singularities. Second, during inspiral, the excision boundaries of the grid remain spherical and do not change shape even though the individual apparent horizons become distorted as the holes approach each other. As the distortion of the apparent horizons increases, the mismatch between the excision boundaries and the apparent horizons eventually leads to a violation of the excision condition, i.e., the condition that all characteristic fields of the hyperbolic system are outgoing (i.e., into the hole) at each excision boundary. Third, the overlapping domain decomposition used during the inspiral is prone to weak instabilities which cause no trouble during the inspiral but drive rapidly growing modes after the solution becomes highly dynamical.

To address these problems, we stop the simulation about 1.5 orbits before merger, and restart with a modified algorithm. We change smoothly to a damped harmonic gauge [49,78,79] which slows down the formation of coordinate singularities. We also dynamically modify the coordinate mapping between the grid frame and the inertial frame so that the excision boundaries conform to the shapes of the apparent horizons [42,49]. Furthermore, by monitoring the characteristic speeds of the system, we dynamically vary the velocity (with respect to the horizon) of each excision boundary so as to ensure that the characteristic fields are outgoing at these boundaries for all times; this characteristic speed control is also crucial for evolving BBHs with large spins [44]. Finally, we run the simulation on a set of nonoverlapping subdomains consisting of topological

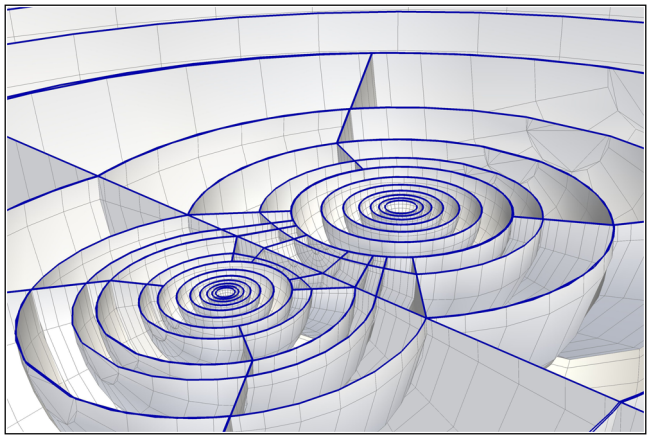

FIG. 3 (color online). Domain decomposition used for the plunge and merger for mass ratio $q = 2$. The thick blue lines represent subdomain boundaries in the $z = 0$ plane. The region $z > 0$ is not shown. Also not shown is the additional deformation of the grid near the black holes that matches the shape of the excision spheres to the apparent horizons.

cubes, cylindrical shells, and spherical shells. This domain decomposition is shown in Fig. 3. Each subdomain is distorted by a coordinate mapping so that the subdomains do not overlap and so that the union of these subdomains covers the entire 3-dimensional region (minus two excised holes) inside a spherical outer boundary $R_{\rm Bdry}$ of order a few hundred M from the source (see Sec. III C 2 where we compare runs with different values of $R_{\rm Bdry}$). More details about the merger domain decomposition are given in the appendix. It avoids certain instabilities which appear for domain decompositions with overlapping grid close to merger [49]. In addition, we choose a slightly higher resolution for the nonoverlapping grid than for the overlapping grid used during inspiral, because the merger has features with a shorter length scale than in the inspiral. After the binary has reached about $t \sim 2M$ before merger, we increase the resolution one last time, particularly in the region between the two holes.[4]

After a common apparent horizon forms, we regrid onto a new set of subdomains consisting of nested distorted spherical shells. The innermost boundary is just inside the common apparent horizon, and conforms to its shape. The outermost boundary is the same $R_{\rm Bdry}$ used in the merger. The matching of the ringdown to the inspiral is discussed in Ref. [49].

F. Relation to other SpEC simulations

Several other SpEC simulations of binary black holes have been presented in the literature [40,42–44,52]. In this section, we briefly describe some computational details common to all SpEC simulations, and we describe how some of the new computational infrastructure presented here relates to these other simulations.

Our apparent horizon finder expands the radius of the apparent horizon as a series in spherical harmonics up to some order L. We utilize the fast flow methods developed by Gundlach [80] to determine the expansion coefficients. The quasilocal spin S of each black hole is computed with the spin diagnostics described in Ref. [81]. We compute the spin from an angular momentum surface integral [82,83] using approximate Killing vectors of the apparent horizons, as described in Refs. [81,84] (see also Refs. [85,86]). We define the dimensionless spin by

$$\chi = \frac{S}{M^2}. \tag{23}$$

We extract gravitational waves from our simulations by two independent methods. We compute the Newman-Penrose scalar Ψ_4 using the same procedure as described in Refs. [51,52]. This involves constructing the correct contraction of the Weyl curvature tensor at several finite-radius coordinate-spheres far from the source and projecting into spin-weighted spherical harmonics. We also extract the Regge-Wheeler-Zerilli (RWZ) [87,88] gravitational wave strain $h_{\ell m}$ as formulated in Ref. [89]. The implementation of this formulation in the SpEC code is described in Ref. [90] (see also Ref. [26] and the appendix of Ref. [25] for further details). Both the Ψ_4 and the RWZ waveforms, which are extracted at a series of finite-radius coordinate spheres, are extrapolated to infinite distance from the source [91]. The Ψ_4 waveforms generally agree well with the (second time derivative of the) RWZ $h_{\ell m}$ waveforms, although for some purposes RWZ is a better choice than Ψ_4 or vice versa. For example, computing strain from Ψ_4 requires two time integrations and careful choice of integration constants, so it is simpler and less error-prone to instead use RWZ to compute strain. Similarly, computing the recoil velocity requires either a time derivative of $h_{\ell m}$ or a time integral of Ψ_4; the time derivative amplifies noise in the waveform, and this affects the recoil velocity enough that it is better to use a time integral of Ψ_4 for that purpose.

In parallel to the present work, superposed Kerr-Schild initial data [81,92,93] have been developed and applied to SpEC simulations of black holes with high spins [40,44]. The algorithmic improvements discussed in the present work are generally compatible with superposed Kerr-Schild simulations. Specifically, the root-finding procedure discussed in Sec. II B can be applied to superposed Kerr-Schild initial data. This requires a change of free parameters from excision sphere radii to masses of the conformal black holes in the superposed Kerr-Schild initial data. Early tests indicate that the root-finding procedure works satisfactorily. However, more exhaustive tests, especially for high spin systems, will be necessary.

[4]The processes of regridding, changing resolution, and changing the coordinate mapping have since been automated; this will be described in a future work.

TABLE I. Runs considered in this paper, with $q = 1$ from Ref. [42] included for completeness. Initial data parameters are orbital frequency Ω_0, the expansion factor $\dot{a}_0$, and the coordinate distance between the black hole centers D_0. Furthermore, the initial and final radii of the outer boundary are given ($R_{\rm Bdry}$ is decreasing during the evolution, cf. Ref. [52]), as well as the initial orbital eccentricity $\varepsilon_{ds/dt}$ and the number of gravitational wave (GW) cycles before the peak of $|h_{22}|$, $N_{\rm GW}$. The last three columns denote the Christodoulou mass, dimensionless spin, and kick velocity of the merged black hole at the end of ringdown.

	Initial Data					$R_{\rm Bdry}$		Inspiral		Remnant properties		
q	$10^3 M\Omega_0$	$10^6 \dot{a}_0 M$	D_0/M	$E_{\rm ADM}/M$	$J_{\rm ADM}/M^2$	$t=0$	$t\to$ late	$10^5\varepsilon_{ds/dt}$	$N_{\rm GW}$	$M_{c,f}/M$	$S_f/(M_{c,f})^2$	$v_{\rm kick}$(km/s)
1	16.7081	−28.40	14.4363	0.992333	1.0857	460M	290M	5	33	0.95162(2)	0.68646(4)	0
2	17.6711	−62.53	13.8738	0.993025	0.9555	444M	442M	3	31	0.96124(2)	0.62344(4)	148(2)
3	18.9994	−63.63	13.1767	0.993868	0.7922	422M	420M	2	31	0.97128(1)	0.54058(2)	174(6)
4	20.3077	−66.08	12.5652	0.994568	0.6655	402M	400M	4	31	0.97792(2)	0.47160(10)	157(2)
6	19.35244	−42.43	13.0000	0.995968	0.5157	572M	569M	4	43	0.98547(5)	0.37245(10)	118(6)

The control system discussed in Sec. II C 1 is applicable to any nonprecessing simulation, independent of the type of initial data. The choice of gauge source functions H_a (equal to the values in the initial data, with appropriate coordinate transformations applied [42,43,52]) does not work for simulations with moderate or large spins; such simulations use active gauge conditions already during the inspiral, see e.g., Ref. [40]. Furthermore, moderate to high spin simulations require use of a nonoverlapping domain decomposition during the inspiral to avoid certain grid instabilities. We have no reason to believe that the more complex and computationally more expensive technology for high-spin systems might fail for the present nonspinning simulations. We have not tested this, because the methods presented here are more efficient for the systems being studied here. Techniques for handling the merger, as described in Sec. II E and the appendix, are common between the high-spin simulations and the simulations presented here.

III. RESULTS

A. Overview

In this section, we present the results of our simulations of nonspinning binary black holes with mass ratios $q = 2$, 3, 4, 6. These simulations contain long inspirals (15 to 22 orbits), merger, and ringdown. To achieve our desired number of inspiral orbits, we compute the initial coordinate separation D_0 using Taylor T3 post-Newtonian predictions [41] and then proceed to the eccentricity removal procedure as explained in Sec. II D. Our final parameters for the initial data set are summarized in Table I, and Fig. 4 shows the trajectories of all our runs through inspiral, the formation of a common apparent horizon, and merger.

B. Mass calibration

A mass scale M by which all data are rescaled is defined as follows. Consider the sum of the two irreducible masses, defined from the areas $A_{\rm AH1}$ and $A_{\rm AH2}$ of the apparent horizons,

$$M_{\rm irr}(t) \equiv \sqrt{\frac{A_{\rm AH1}(t)}{16\pi}} + \sqrt{\frac{A_{\rm AH2}(t)}{16\pi}}. \tag{24}$$

Root finding during construction of the initial data ensures $M_{\rm irr}(0) = 1$. Figure 5 presents convergence data for the irreducible mass during the simulations. Plotted is the relative change of $M_{\rm irr}(t)$. Convergence is clearly apparent, and the irreducible mass is constant to within a few parts in 10^6 at the highest resolution, except immediately before merger. During the first $\sim 100M$, the black hole mass increases by about 1×10^{-6}. Since this is below the numerical error during inspiral shown in Fig. 5, we define our mass scale by

$$M \equiv M_{\rm irr}(0) \tag{25}$$

for all mass ratios.

C. Accuracy

1. Phase convergence

One of the goals of the present work is to calculate long, accurate waveforms for the dominant and top subdominant

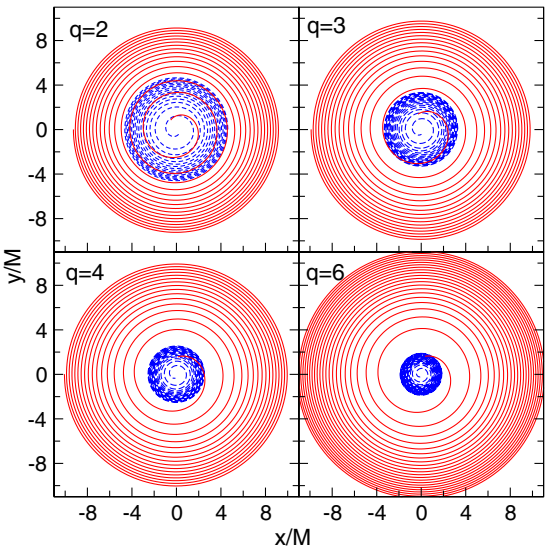

FIG. 4 (color online). Orbital trajectories for mass ratio $q = 2$, 3, 4, 6. For all mass ratios, the trajectory of the larger hole is represented by a dashed blue line, and that of the smaller hole by a solid red line.

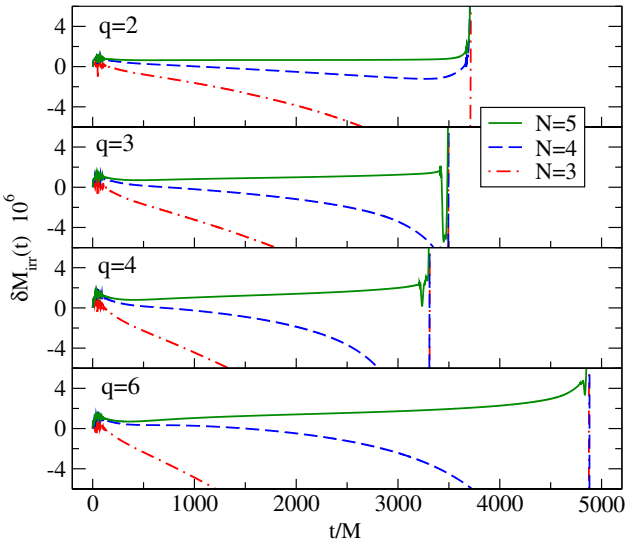

FIG. 5 (color online). Convergence of the irreducible mass. Plotted is $\delta M_{\rm irr} \equiv [M_{\rm irr}(t) - M_{\rm irr}(0)]/M_{\rm irr}(0)$ for three different numerical resolutions ($N = 3, 4, 5$).

gravitational wave modes—(2,2), (3,3), and (2,1)—from unequal-mass binary black hole simulations. The top subdominant modes are those with the largest peak strain amplitude. To determine the accuracy of these waveforms, we perform convergence studies of RWZ-$h_{\ell m}$ at a particular extraction radius.

All simulations are run at three different resolutions, labeled $N = 3, 4, 5$. For all three resolutions, the RWZ gravitational waveforms at a finite extraction radius ($R_{\rm ext} = 338M$ for $q = 2, 3, 4$ and $R_{\rm ext} = 460M$ for $q = 6$) are computed. We decompose the complex spherical harmonic modes into real-valued amplitude and phase:

$$h_{lm}(t) = A_{lm}(t)\exp(i\phi_{lm}(t)). \tag{26}$$

We next compute differences $\Delta\phi_{lm}(t)$ between different resolutions *without* any time shifts,

$$\Delta\phi^{NN'}_{lm}(t) = \phi^{N}_{lm}(t) - \phi^{N'}_{lm}(t), \tag{27}$$

where the superscripts N and N' refer to the numerical resolutions being considered. Finally, for ease of presentation, we time-shift the phase differences to align convergence tests of different mass ratios at their respective times of peak amplitude of the h_{22} mode, $t_{\rm peak22}$.

Phase differences for the dominant (2,2) mode are plotted in Fig. 6. Note that this figure shows only the part of the simulation around merger time. During the earlier inspiral, the phase errors are lower. It is apparent from this plot that the phase accuracy deteriorates with increased mass ratio, albeit quite slowly. This is expected, as simulations become numerically more difficult with increased mass ratio, owing to the smaller GW flux, and the smaller length scale of the small black hole. Nevertheless, the phase accuracies of all the new simulations presented in this paper are comparable to that of the equal-mass, zero spin

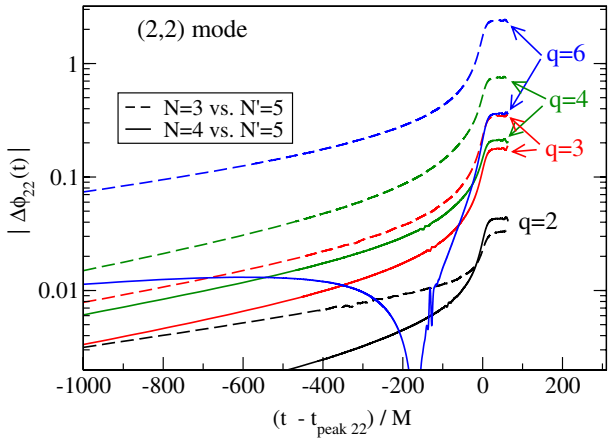

FIG. 6 (color online). Phase convergence of RWZ-h (2,2) modes for inspiral-merger-ringdown waveforms. Shown are the phase differences between a given resolution and the highest resolution.

simulation presented in Scheel *et al.* [42], with the simulations at low mass ratios ($q = 2$) being somewhat more accurate, and those at higher mass ratios ($q = 3, 4, 6$) somewhat less accurate.

Note that during merger and ringdown, the three resolutions of the $q = 2$ simulation do not follow the usual pattern indicating convergence. There are a few possible reasons for this. One is that for $q = 2$, the truncation error as a function of resolution may change sign near one of the resolutions $N = 3$, 4, or 5, thus producing an artificially small truncation error and skewing the test shown in Fig. 6. Another possibility is that the unusual pattern is caused by small differences in gauge or domain decomposition between different resolutions: as explained in Section II E, we change the gauge and domain decomposition about 1.5 orbits before merger, but these changes occur at slightly different times for different resolutions, and this time offset will introduce a small nonconvergent error. Note also that the $q = 2$ case appears to have a factor of three smaller truncation error than any previous long SpEC simulation, so this case may reveal small error sources that may not have been evident in previous simulations. Figure 6 shows a feature in the $q = 6$ simulation around $t \sim -180M$. This arises because the phase difference between $N = 4$ and $N = 5$ simulations changes sign.

Convergence tests for the two leading subdominant modes (2,1) and (3,3) are presented in Fig. 7. During the inspiral, the phase errors of the (2,1) mode are approximately half as large as those for the (2,2) mode, whereas the errors in the (3,3) mode are approximately a factor 1.5 larger. This scaling is reasonable, as all three GW modes are determined primarily by the orbital phase evolution. The gravitational wave mode (l, m) proceeds through m cycles for each orbit; hence, the GW phase errors of different modes should be proportional to m. During merger and ringdown, the observed phase errors behave differently:

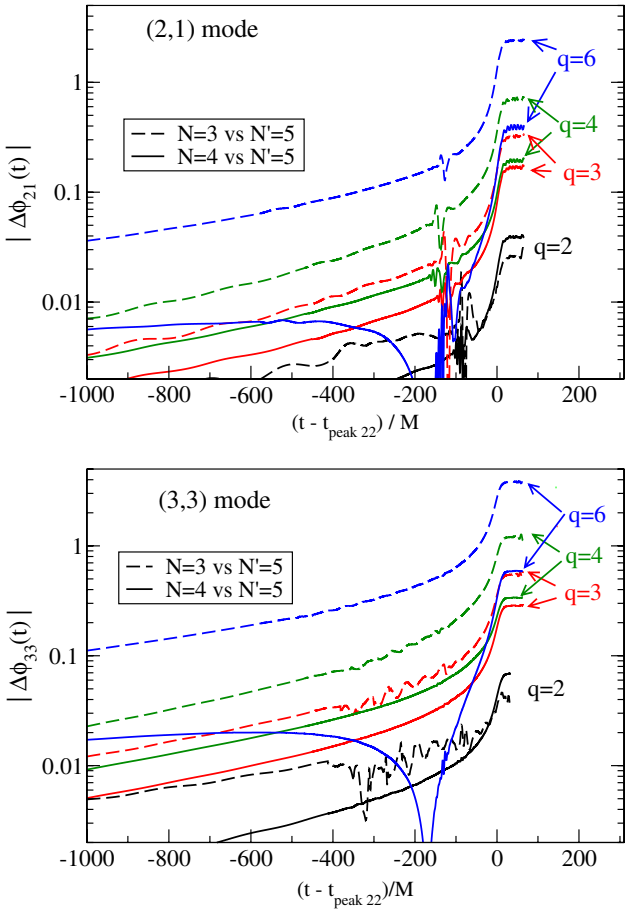

FIG. 7 (color online). As Fig. 6, but for the subdominant modes (3,3) and (2,1).

$\Delta\phi_{33}$ is larger than $\Delta\phi_{22}$ for all mass ratios, whereas $\Delta\phi_{21}$ is similar in amplitude to $\Delta\phi_{22}$. Figure 7 shows noise in the (2,1) convergence test, starting about $150M$ before peak amplitude. Presumably, the noise in the phase is more prominent in the (2,1) mode because of the small amplitude of this mode.

2. *Effect of location of outer boundary*

The simulations presented here are of such long duration that the black holes are in causal contact with the outer boundary for a large portion of the evolution. The question therefore arises: are the results affected by our choice of outer boundary conditions? Ideally, the gravitational waveforms computed on a truncated computational domain with an artificial outer boundary should not have errors introduced by the boundary conditions themselves—either from spurious reflections of gravitational radiation or from constraint violations at the outer boundary. The extent to which this is achieved indicates the degree to which the outer boundaries are "absorbing" (see e.g., Refs. [64,72,73,90]). The outer boundary conditions used in our simulations are (i) constraint-preserving and (ii) freeze the Weyl scalar Ψ_0 to its initial value. These "semiabsorbing" boundary conditions are the simplest in a hierarchy of increasingly absorbing boundary conditions, described in detail in Sec. 4.2 of Ref. [72].

TABLE II. Radii of the outer boundary for the runs with different outer boundary locations (in units of the initial separation D_0). Also given is the ratio Q of spurious reflections from the (2,1) mode relative to those from the (2,2) mode, cf. Eq. (29).

q	$R_{\rm close}$	$R_{\rm normal}$	$R_{\rm far}$	$Q_{m=1,m=2}$
2	$20D_0$	$32D_0$	$50D_0$	0.54
3	$20D_0$	$32D_0$	$50D_0$	0.80
4	$20D_0$	$32D_0$	$50D_0$	1.02
6	$26D_0$	$44D_0$	$74D_0$	1.14

To evaluate the impact of the artificial outer boundary on our simulations, we repeat the $N = 4$ simulations for each mass ratio with two additional outer boundary radii, $R_{\rm close}$ and $R_{\rm far}$, where the distance to the outer boundary is changed *only* by adding or removing outer spherical shells in our domain decomposition. The different outer boundary radii are listed in Table II. The h_{22} waveforms are extracted from these simulations, and phase differences between runs with different outer boundary radii are computed and plotted in Fig. 8. The plotted phase differences are oscillatory during inspiral, indicating that the runs being compared have slightly different orbital eccentricities. Around merger, a systematic phase difference appears of a few times 0.01 rad for the near boundary

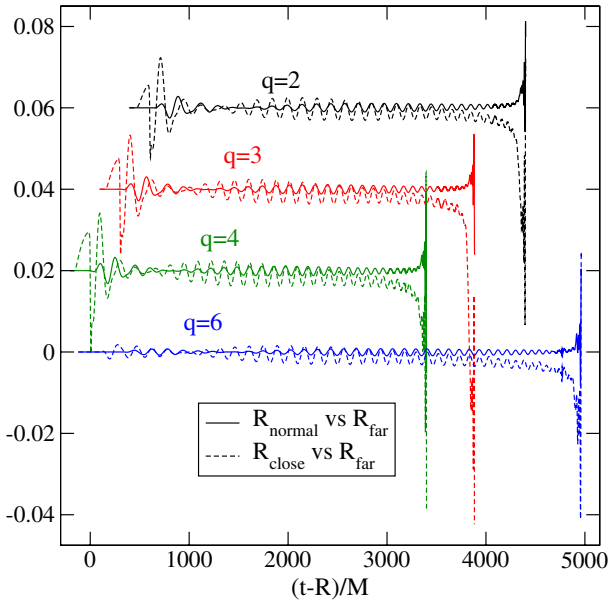

FIG. 8 (color online). Effect of the outer boundary location. Shown are phase differences of h_{22} between simulations with outer boundary radii given in Table II. The solid lines give the differences between "normal" and "far" boundaries; the dashed lines give the differences between "close" and far boundaries. For clarity, $q = 2$, 3, 4 are offset vertically by multiples of 0.02 rad, and $q = 2$, 3 are offset horizontally by multiples of $300M$. R denotes the extraction radius of each simulation.

and $\lesssim 0.005$ rad for the normal boundary location. During ringdown, the gravitational wave amplitude decays exponentially, and the calculation of the phase becomes increasingly noisy. We truncate the plotted data when the amplitudes of the waves have decayed to 1% of their peak values. It is evident from Fig. 8 that the transparency of the outer boundary diminishes as the distance to the boundary decreases. For our "normal" boundary radius, the phase error due to the boundary is $\lesssim 0.005$ rad (when compared to the far location), which is negligible relative to the truncation error presented in Fig. 6. On the other hand, moving the boundary from the normal to the close location increases phase errors 5 to 10 times. We can relate the phase errors reported in Fig. 8 to the expected reflection coefficients of our semiabsorbing boundary conditions as analyzed in Ref. [72]. The quadrupolar wave ($\ell = 2$) reflection coefficient σ_2 for freezing Ψ_0 plus constraint preserving boundary conditions is given by Eq. (89) of Ref. [72]. In the limit of large boundary radius $kR_{\rm Bdry} \gg 1$ (where k is the wave number of the outgoing wave), the reflection coefficient reduces to

$$\sigma_2 = \frac{3}{2}(kR_{\rm Bdry})^{-4}. \tag{28}$$

"Near" boundaries are a factor $\sim$1.6 closer than normal boundaries; therefore, the reflection coefficient will be larger by a factor $1.6^4 \approx 6.5$, consistent with the observed increase of phase errors by a factor 5–10 in Fig. 8. Moreover, according to an argument given in Ref. [94], the phase error due to reflection of the (2,2) mode of the outgoing radiation should be roughly equal to σ_2 times the total accumulated phase.[5] For the $q = 2$, 3, 4 simulations with normal boundary locations, we have $kR_{\rm Bdry} \sim 18$ and $\sigma_2 \sim 1.3 \times 10^{-5}$. The $\sim$30 GW cycles of inspiral correspond to $\phi_{22} \sim 200$ rad, so that $\sigma_2\phi_{22} \sim 0.003$ rad, in broad agreement with Fig. 8.

For unequal-mass BBHs, it is important to consider reflection coefficients for higher-order modes, since the amplitude of these modes relative to the dominant (2,2) mode increases with mass ratio (see Fig. 10). For example, the reflection coefficients for both the (2,1) mode and the (2,2) mode are given by Eq. (28), but the (2,1) mode has twice the wavelength of the (2,2) mode, reducing $kR_{\rm Bdry}$ by a corresponding factor of 2. Consequently the reflection coefficient σ_{21} of the (2,1) mode is a factor $2^4 = 16$ times larger than the reflection coefficient σ_{22} of the (2,2) mode. If we assume that the impact on the phase error is proportional to the amplitude of the reflected waves, then the relative importance of reflections of the (2,1) mode and the (2,2) mode is given by the ratio

$$Q_{m=1,m=2} \equiv \frac{A_{21}\sigma_{21}}{A_{22}\sigma_{22}}, \tag{29}$$

where A_{21} and A_{22} are the amplitudes of the (2,1) and (2,2) modes, respectively. Note that in the limit of large radii, $Q_{m=1,m=2}$ is independent of boundary radius (because $R_{\rm Bdry}$ cancels out of the ratio σ_{21}/σ_{22}) and independent of GW extraction radius (because the extraction radius cancels out of the ratio A_{21}/A_{22}). Looking up the amplitudes of the (2,1) and (2,2) modes from Fig. 10 and using $\sigma_{21}/\sigma_{22} = 16$ results in the numerical values shown in Table II (note that for these calculations, the amplitudes were taken at a specific time during the inspiral when they are still fairly constant). From this table, we conclude that with our semiabsorbing (constraint preserving plus freezing Ψ_0) boundary conditions, the impact of the (2,1) reflections on the overall phase error is comparable to that of the (2,2) reflections, especially as the mass ratio increases to $q = 4$ or higher. With boundary conditions that are less than semiabsorbing, the error contributions would be even higher.

D. Properties of gravitational radiation

Figure 9 shows the waveforms for our 15-orbit inspiral, merger, and ringdown, as measured by $(R/M)h_{\ell m}$. All these waves have been extrapolated to infinity. We show the top three modes: (2,2), (3,3), (2,1). Notice that the amplitude of the (2,2) mode decreases as the mass ratio increases, but the amplitudes of the other modes stay approximately the same, further notice that the wavelength of the (2,1) mode is about twice that of the (2,2) mode. This is a general property: for a given ℓ, the wavelength of the waveform is typically proportional to $1/|m|$.

The relative importance of the (3,3) and (2,1) mode amplitudes to that of the (2,2) mode is shown for the inspiral and merger in Fig. 10 [top panel: (3,3) mode, bottom panel: (2,1) mode]. This figure clearly shows that the higher-order modes grow in relative significance as the mass ratio increases. At frequency $M\omega_{22} = 0.06$, the ratio A_{33}/A_{22} ranges from 0.08 (for $q = 2$) to 0.16 (for $q = 6$), and A_{21}/A_{22} from 0.04 (for $q = 2$) to 0.08 (for $q = 6$). At the peak of the h_{22} waveform (indicated by the filled circles in Fig. 10), $A_{33}/A_{22} = 0.14$ for $q = 2$ and 0.28 for $q = 6$; $A_{21}/A_{22} = 0.09$ for $q = 2$ and 0.20 for $q = 6$.

E. Black hole spin and tidal spin up

We measure black hole spins by a surface integral on the apparent horizon which utilizes approximate Killing vectors computed from a minimization principle [81]. We denote the dimensionless spin by $\chi_A = S_A/M_A^2$ where $A = 1$ indicates the more massive black hole, and $A = 2$ the less massive one. At $t = 0$, both black hole spins are very small: $\chi_i(t = 0) < 10^{-8}$. This is expected since $\chi_A = 0$ is enforced as part of the initial data construction, cf. Sec. II B. During the initial relaxation of the initial data, the black hole spins increase to a few parts in 10^{-7}. Subsequently, χ_1 slowly increases during the inspiral (with spin rotation axis parallel to the orbital angular

[5] Depending on assumptions, σ_2 may be raised to a power close to unity, cf. Eq. (17) of Ref. [94].

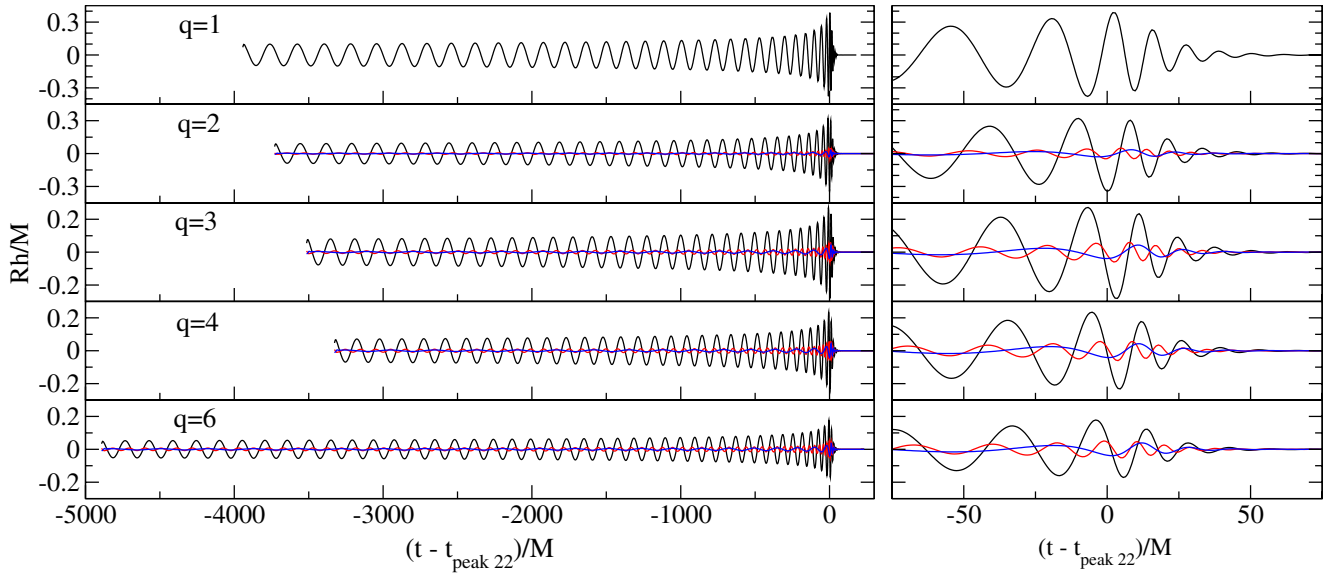

FIG. 9 (color online). Gravitational waveforms for $q = 1, 2, 3, 4, 6$ that have been extrapolated to infinity. Shown are the h_{22} mode (black, large amplitude), h_{33} mode (red, small amplitude and short wavelength), and the h_{21} mode (blue, small amplitude and long wavelength). Only the real parts have been plotted. The x axis has been time-shifted so that 0 indicates the merger, as determined by the peak of the extrapolated h_{22} mode waveform, for each mass ratio. The left-hand panels show the full coalescence: inspiral, merger, ringdown. The right-hand panels show a close up of the merger and ringdown. Only the h_{22} mode is shown for $q = 1$, since the odd-m modes do not appear here.

momentum). This increase is convergently resolved, as shown in the left panel of Fig. 11. In contrast, the spin of the smaller black hole χ_2 remains closer to zero, as shown in the right panel if Fig. 11. For mass ratios $q = 3, 4, 6$, χ_2 is consistent with zero within truncation error. For $q = 2$, there is a marginal detection of nonzero spin at late times $t \gtrsim 3000M$.

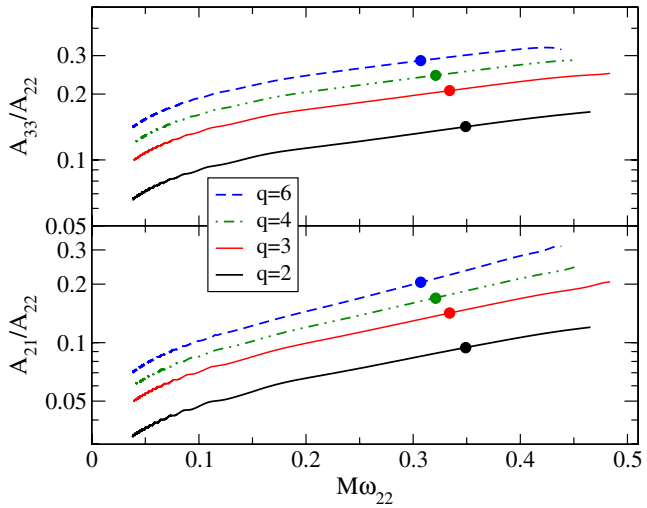

FIG. 10 (color online). Amplitudes of h_{33} (top) and h_{21} (bottom) modes, normalized by the amplitude of the leading h_{22} mode, for mass ratios $q = 2, 3, 4, 6$. Relative amplitudes are plotted vs the frequency of the h_{22} mode. The filled circles indicate the frequencies where the amplitude of the h_{22} mode peaks.

We interpret the monotonically increasing spin χ_1 as evidence of tidal spin up of nonrotating black holes. To investigate this process in more detail, we consider the spin χ_1 as a function of the orbital frequency. Alvi [95] derived tidal spin up as a function of binary coordinate separation b/M. Converting his formula into a function of the orbital frequency (which heuristically should be less gauge-dependent) via $M/b = (M\Omega)^{2/3}$, one obtains

$$\chi_1 - \chi_{1,\infty} = \frac{\eta M_1}{4M}(1 + 3\chi_{1,\infty}^2)\left(-\frac{\chi_{1,\infty}}{4}(M\Omega)^{4/3} + \frac{2r_{1,\infty}}{7M}(M\Omega)^{7/3}\right). \quad (30)$$

$\chi_{1,\infty}$ is the spin magnitude of black hole 1 at infinite separation, and $r_{1,\infty} = M_1(1 + \sqrt{1 - \chi_{1,\infty}^2})$ is the corresponding horizon radius. Dropping terms quadratic in $\chi_{1,\infty}$ because of their small size, this equation simplifies to

$$\chi_1 = \chi_{1,\infty}\left(1 - \frac{\eta M_1}{16M}(m\Omega)^{4/3}\right) + \frac{\eta M_1^2}{7M^2}(m\Omega)^{7/3}. \quad (31)$$

Furthermore, the expression in parentheses in the first term on the right-hand side is so close to unity that the deviation from unity is irrelevant given the small value of $\chi_{1,\infty}$. Approximating this parenthesis by unity, we finally find

$$\chi_1 = \chi_{1,\infty} + f_1(M\Omega)^{7/3} \quad (32)$$

with the coefficient

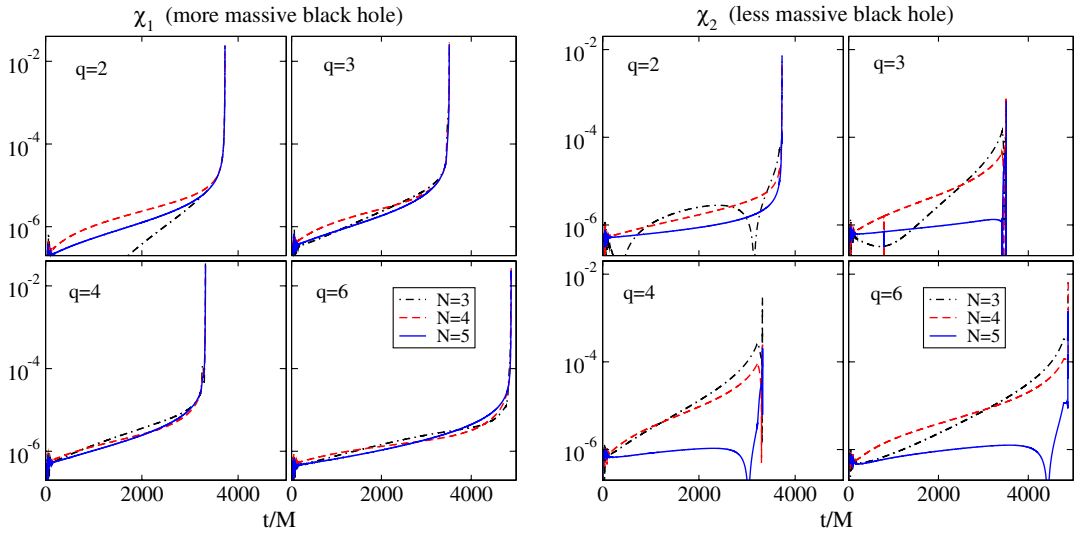

FIG. 11 (color online). Convergence test of the dimensionless black hole spins $\chi = S/M^2$. The left panel shows data for the more massive black hole, the right panel for the less massive black hole. For each mass ratio, three resolutions are shown, labeled $N = 3, 4, 5$. The spin of the more massive black hole, χ_1 is convergently resolved and is monotonically growing during the simulation. The spin of the smaller black hole χ_2, is consistent with $\chi_2 = 0$ within numerical errors.

$$f_1 = \frac{\eta M_1^2}{7M^2} = \frac{q^3}{7(1+q)^4}. \tag{33}$$

Therefore, we see that the spin $\chi_1(M\Omega)$ should follow a power law in frequency $M\Omega$.

The magnitude of the change in the spin is determined by the coefficient $f_1(q)$, which is plotted in Fig. 12. The red circles denote the values of this coefficient for the large black hole in our simulations: The mass ratios considered here all result in almost maximal tidal coupling, for maximal spin up of the large black hole. In contrast, the black crosses denote the spin coupling coefficient for the small black hole. The spin coupling coefficient for the small black hole is smaller by a factor between 4 ($q = 2$) and 36 ($q = 6$), indicating that the smaller black hole will be much less susceptible to tidal spin up. Therefore, from the perturbative analysis of tidal coupling, we expect that the larger black hole in all our simulations will be spun up by approximately similar amounts, and that the small black hole will be spun up significantly less. This expectation is already borne out in Fig. 11, where we were able to resolve the spin up of BH 1, but not the (smaller) spin up of BH 2.

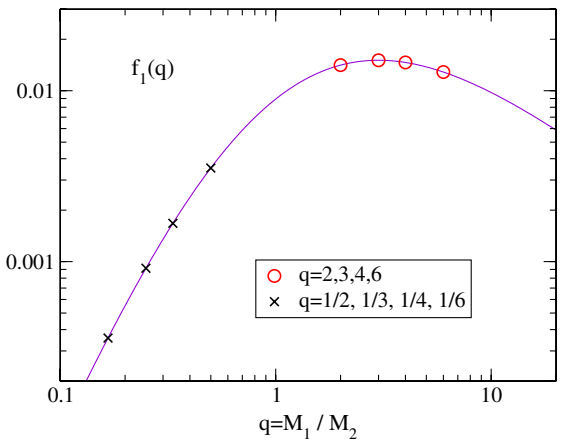

FIG. 12 (color online). The coupling coefficient f which determines the magnitude of the change of the spin χ_1 during the inspiral as a function of the mass ratio $q = M_1/M_2$. The red circles denote the coefficients for the large black hole for the mass ratios simulated here. The crosses denote the coefficient for the small black hole, which can be obtained from the same plot at the inverse mass ratio.

Fitting the numerical data $\chi_1(M\Omega)$ to the functional form of Eq. (32) with the one free fitting parameter $\chi_{1,\infty}$ results in a moderately good fit. The fit can be improved if the coefficient f_1 is also fitted for, and can be improved further by also allowing the exponent to vary, i.e., a power-law fit with an offset. The results of these fits (which we refer to as fit 3, fit 2, and fit 1, respectively), are shown in Table III. Figure 13 plots the fits and their residuals for mass ratios $q = 2$ and $q = 6$. All fits were performed over the numerical data up to orbital frequency $M\Omega = 0.055$.[6] As can be seen from the insets of Fig. 13, the more general fit 1 is superior to a fit with fixed exponent $7/3$ (fit 2), which in turn is superior to the one-parameter fit 3 of Eq. (32). For $q = 2$, the residual of fit 1 is almost two orders of magnitude smaller than for fits 2 and 3. Coefficient A_2 in Table III shows that the numerical data prefers a power law with a slightly *larger* exponent of roughly $8/3$ instead of the expected $7/3$. If the exponent is fixed to $7/3$, then coefficient B_1 indicates that the overall

[6]Beyond this frequency, we modify the gauge in the simulation, which leads to artifacts in $\chi_1(\Omega M)$.

TABLE III. Fitting parameters for fits to the $\chi_1(M\Omega)$ data.

	Fit 1 $A_0 + A_1(M\Omega)^{A_2}$			Fit 2 $B_0 + B_1 f_1(M\Omega)^{7/3}$		Fit 3 $C_0 + f_1(M\Omega)^{7/3}$
q	$10^6 A_0$	A_1	A_2	$10^6 B_0$	B_1	$10^6 C_0$
2	−0.95	0.0362	2.57	−1.26	1.23	−0.88
3	−1.10	0.0496	2.64	−1.59	1.29	−0.99
4	−1.25	0.0474	2.62	−1.78	1.34	−0.96
6	−0.81	0.0602	2.74	−1.39	1.34	−0.74

magnitude of the spin evolution is larger in the numerical simulation by about a factor of 1.3 relative to the expected behavior Eq. (32). All fits indicate fairly consistently that the spin of the large black hole at infinite separation would be around 10^{-6}, antialigned with the orbital angular momentum (cf. coefficients A_0, B_0, C_0).

These results are enticing and suggestive. However, we caution the reader that the observed effects are very small, with changes to the dimensionless spin of order 10^{-5}.

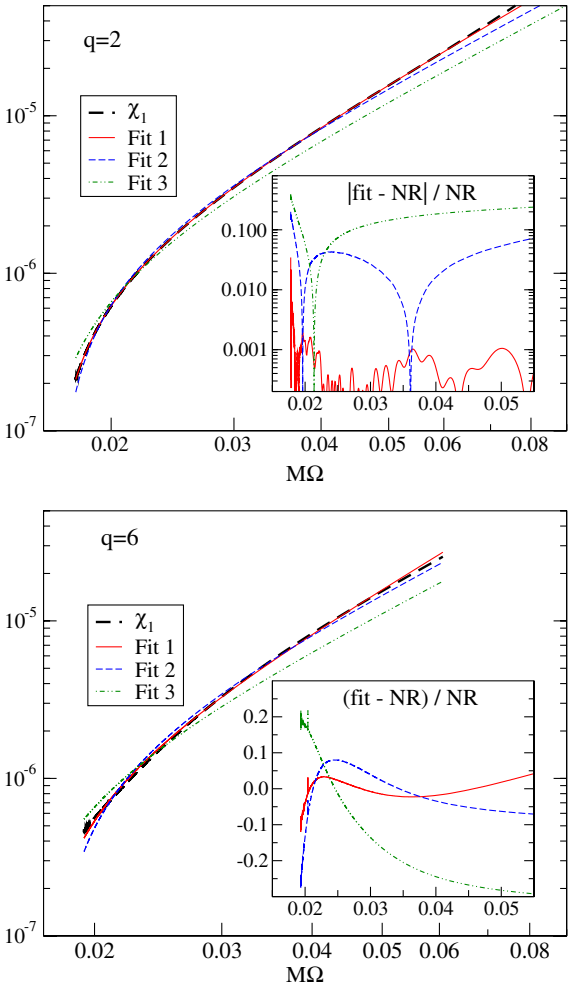

FIG. 13 (color online). Dimensionless spin χ_1 of the larger black hole as a function of the orbital frequency $M\Omega$. Plotted is the numerical data, and three fits to the data, fitted in the interval $M\Omega \leq 0.055$.

Before drawing firm conclusions, one must establish that the numerical data is accurate enough by performing a threefold convergence test. First, the resolution of the numerical evolution must be varied to determine that Einstein's equations are solved with sufficient accuracy. This we have done. However, in addition to this numerical convergence test, the resolution of the apparent horizon finder must be varied to ascertain that the apparent horizon is found with adequate accuracy. And finally, the resolution of the eigenvalue solver that computes the approximate helical Killing vectors on the apparent horizon (cf. the appendix of Ref. [81]) must be varied to check that the approximate Killing vectors are calculated accurately enough. Unfortunately, we did not output enough data during the numerical evolutions to perform the second two convergence tests.

In addition, further work would be needed to ascertain that the approximate Killing vectors (and the spin computed using these, cf. Ref. [81]) are indeed generating a spin compatible with the spin definitions of the perturbative work [95]. Because of all these cautionary comments, and insufficient numerical data, we postpone quantitative results about tidal spin up to future work.

F. Remnant properties

Figures 14 and 15 show the mass and spin of the remnant black hole (computed using approximate Killing vectors on the apparent horizon [81,84–86]) as a function of mass ratio q. These quantities are also listed in Table I. Several fitting formulas in the literature give good agreement with the remnant spin and are plotted in Fig. 15. Analytical predictions of the final mass do not agree as quite as well, as seen in Fig. 14; however, the formula of Buonanno *et al.* [17], which is a fit to numerical relativity results, shows better agreement.

For unequal-mass binaries, linear momentum is carried off anisotropically by gravitational waves, leading to a recoil of the remnant black hole. The recoil speed of the remnant can be computed from the gravitational-wave momentum flux at infinity. To do this, we start with the Newman-Penrose quantity Ψ_4, extracted from our simulations and extrapolated to infinite radius using the procedure of Boyle and Mroué [91]. The momentum flux depends on the first time integral of Ψ_4, and computing this time integral requires two integration constants, which we determine by the

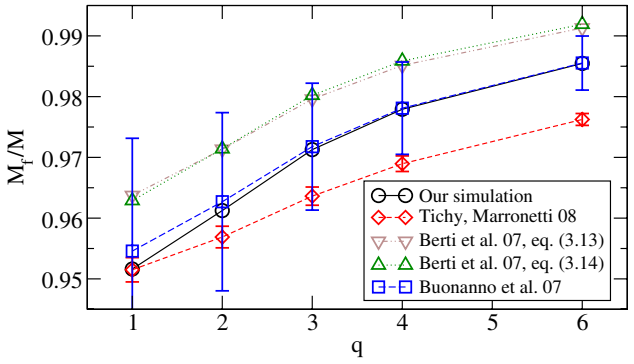

FIG. 14 (color online). M_f/M as function of q. Also shown are the results from the fitting formula of Tichy and Marronetti [100], the analytical prediction of Berti *et al.* [99], and the fit of Buonanno *et al.* [17] to numerical data.

procedure outlined in Appendix B of Ref. [96]. This procedure involves a minimization over a time interval $[t_1, t_2]$, where t_1 and t_2 can be chosen arbitrarily. We find that varying the integration-constant parameters t_1 and t_2 in the range $t_1 \in [1000M, 1400M]$ and $t_2 \in [2600M, 3000M]$ changes $v_{\rm kick}$ by only a tenth of a percent. Once we have the time integral of Ψ_4, we compute the gravitational-wave momentum flux by the procedure of Ref. [97], keeping all $Y_{\ell m}$ modes through $\ell = 6$.The time integral of the momentum flux gives the total radiated 3-momentum $\vec{P}$, and the recoil velocity is $\vec{v} \equiv -\vec{P}/M_f$. Note that the recoil velocity can alternatively be computed by a time derivative of the Regge-Wheeler-Zerilli strain $h_{\ell m}$ rather than a time integral of Ψ_4. We use the latter method because differentiation amplifies noise in the waveform to the extent that for the runs shown here, the former method would require smoothing put in by hand.

The recoil speed $v_{\rm kick} \equiv |\vec{v}|$ of the remnant is listed in the last column of Table I. We estimate several sources of uncertainty, which are listed in Table IV. Numerical truncation error is estimated by taking the difference of $v_{\rm kick}$ computed using the highest and second-highest numerical resolutions; this is the dominant source of error for two of our simulations. The uncertainty in extrapolating the waveform to infinity is estimated by comparing $v_{\rm kick}$ computed using waves extrapolated using 3rd-order polynomials [91] vs an identical calculation using 4th-order polynomials. The error associated with truncating $Y_{\ell m}$ modes for $\ell > 6$ in the momentum flux is estimated by comparing with an identical calculation where we retain only $\ell \leq 5$. Initial data effects such as the initial pulse of junk radiation add a spurious recoil of about 1 to 2 km/s, depending on the run. There is an additional small error that results from neglecting the recoil that occurs in the early inspiral between $t = -\infty$ and the start of our simulations; this neglected recoil can be estimated to 2 post-Newtonian order using Eq. 22 of Ref. [98], which yields about 0.5 km/s for the cases shown here. Figure 16 plots the recoil vs mass ratio for our simulations and for two fitting formulas in the literature. We find good agreement.

TABLE IV. Recoil velocity and uncertainties in km/s. Uncertainties (left to right) are numerical truncation error, error in extrapolating waveforms to infinity, the effect of using only a finite number of $Y_{\ell m}$ modes to compute the momentum flux, error involving initial transients (e.g., junk radiation), and the estimated recoil accumulated from $t = -\infty$ to the start of our simulation.

q	$v_{\rm kick}$	$\delta v^{\rm T}_{\rm kick}$	$\delta v^{\rm E}_{\rm kick}$	$\delta v^{Y_{\ell m}}_{\rm kick}$	$\delta v^{\rm ID}_{\rm kick}$	$\delta v^{t\to\infty}_{\rm kick}$
2	148	0.7	0.4	1	1	0.4
3	174	6	0.4	0.2	2	0.6
4	157	1.2	0.4	0.3	2	0.6
6	118	4.5	1	3	1	0.4

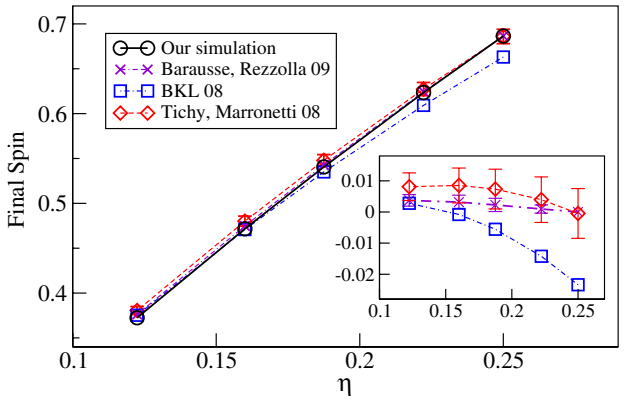

FIG. 15 (color online). S_f/M_f^2 as function of symmetric mass ratio η. Also shown are the results of fitting formulas and estimates from Barausse and Rezzolla [101], from Buonanno, Kidder and Lehner [102], and from Tichy and Marronetti [100]. The inset shows the difference $\chi_{\rm fit} - \chi_{\rm NR}$ between fitting formula and our numerical results.

IV. DISCUSSION

This paper accomplishes several tasks with regard to simulations of BBH systems. Section II B introduces an

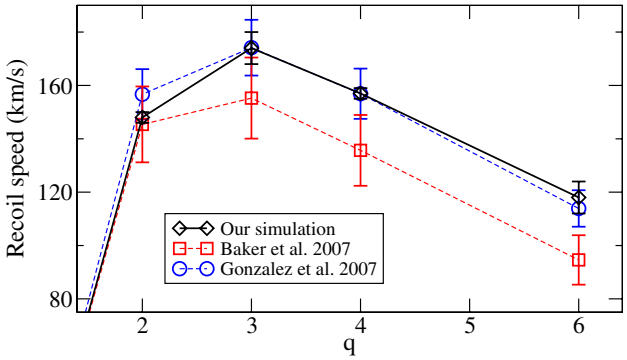

FIG. 16 (color online). $|v_{\rm kick}|$ as function of q. Also shown are the results of fitting formulas and estimates from Baker *et al.* [103] and from Gonzalez *et al.* [14].

efficient formalism to perform root finding necessary to achieve desired initial data parameters (masses, spins, center-of-mass frame). Each function evaluation during root finding is an entire (expensive) initial-data solve, so it is imperative to be able to perform this procedure with as few function evaluations as possible. The procedure introduced here, based on approximate Newton-Raphson iteration, performs very well. As Fig. 1 shows, one or two high-resolution initial data runs are sufficient. Since the high-resolution solutions dominate the overall CPU cost, root finding can thus be accomplished with marginal extra cost. This procedure has since then been extended to superposed Kerr-Schild data [81].

We then give technical details about how to simulate unequal-mass binaries with multidomain spectral methods. In particular, we extend the dual-frame formalism and control systems to unequal masses, introduce eccentricity removal for unequal-mass binaries, and describe algorithmic modifications performed during merger and ringdown.

The largest part of this paper documents a new series of unequal-mass, nonspinning BBH simulations with mass ratios $q = 2$, 3, 4 and 6, lasting between 15 and 22 orbits before merger. We show that these simulations have high accuracy, comparable to that of the equal-mass simulation presented in Refs. [42,52]. The total mass is conserved during the inspiral to a few parts in 10^6 (cf. Fig. 5), a convergence test on the (not-time-shifted gravitational wave phase) indicates that errors in our second-highest resolution run are a few tenths of a radian. Given how much more challenging a mass-ratio 6 simulation is, we are very encouraged that the errors are only larger by a factor of 4 relative to the equal-mass simulation, cf. Fig. 6. By moving the outer boundary, we establish furthermore that effects due to the outer boundary arise at the smaller level of $\sim$0.01 rad in the waveform, as shown in Fig. 8. We also perform a convergence study on the subdominant (3,3) and (2,1) modes of the gravitational radiation. These subdominant modes become more important with higher mass ratio (see Refs. [21,99] and Fig. 10), and we argue that this increases the need for reflection minimizing boundary conditions, as those applied here. The final waveforms, extrapolated to infinite extraction radius, are shown in Fig. 9.

We then consider carefully the change in the spin of the larger black hole. This change is broadly consistent with perturbative calculations of black holes: The power law of the spin vs orbital frequency is rather well-matched (~ 2.66 vs $7/3$), and the amplitude of the change is also reasonably close, being off by a factor $\sim$1.3. A more detailed comparison must, however, await more complete convergence data, to allow comprehensive quantification of the error in the numerical spin. But nevertheless, these data point to the fact that our simulations are in fact for a BBH where the larger black hole started at infinite separation with a spin of $\sim 10^{-6}$ *antialigned* to the orbital momentum. Tidal spin up increases this spin during the early (not modeled) inspiral, so that the spin passes through zero when our simulations commence.

Finally, we compare remnant properties and kick velocities. These are found to be in reasonable agreement to various fitting formulae in the literature.

An important result of this work is the accurate calculation of long *subdominant* mode waveforms. These are needed for parameter estimation, calculating physical quantities such as the gravitational recoil, and for modeling analytic and phenomenological waveforms (see Ref. [21] and references therein). Furthermore, recent results indicate that they are important for LIGO event detection: Brown, Kumar and Nitz (in prep 2012) have found that for $q > 1.8$, the top subdominant modes must be taken into account in order to achieve the usual signal-to-noise ratio loss criterion ''overlap greater than 0.965.'' Pertinent factors used in these simulations which have contributed to the achieved accuracy are: (i) our use of semiabsorbing boundary conditions combined with the location of the outer boundary, (ii) extrapolation to infinity, (iii) good numerical resolution because of the length scale problem (which becomes more severe for the subdominant modes), and (iv) pseudospectral methods. In sum, we have been able to perform the first long and accurate numerical simulations of unequal nonspinning binary black holes with mass ratios as high as 6, with excellent convergence and modest computational cost, even for the subdominant modes.

ACKNOWLEDGMENTS

We would like to thank Enrico Barausse, Duncan Brown, and Abdul Mroué for useful discussions, and Michael Boyle and Fan Zhang for performing wave extrapolations. We are also very grateful to the referee for his or her thorough reading and thoughtful suggestions. This work was supported in part by grants from the Sherman Fairchild Foundation to Caltech and Cornell and by NSF Grants No. PHY-1068881 and No. PHY-1005655 and NASA Grant No. NNX09AF97G at Caltech. H. P. gratefully acknowledges support from the NSERC of Canada, from the Canada Research Chairs Program, and from the Canadian Institute for Advanced Research. Computations were performed on the Syracuse University Gravitation and Relativity (SUGAR) Cluster, which is supported by Syracuse University and NSF Grant No. PHY-0600953; on the NSF XSEDE network under Grant No. TG-PHY990007N; on the Zwicky cluster at Caltech, which is supported by the Sherman Fairchild Foundation and by NSF Grant No. PHY-0960291; and on the GPC supercomputer at the SciNet HPC Consortium [104]. SciNet is funded by: the Canada Foundation for Innovation under the auspices of Compute Canada; the Government of Ontario; Ontario Research Fund–Research Excellence; and the University of Toronto.

APPENDIX: NONOVERLAPPING SPECTRAL GRID

In our spectral evolution code, the use of overlapping grids sometimes leads to weak instabilities. We find that these instabilities can be cured by use of nonoverlapping grids. There are a number of choices one has to make while designing such a grid. A basic assumption is that at some distance from the center the geometry of the spacetime is close to spherical symmetry. Spherical shells are our most efficient grid structure to represent such a region. In the near zone (around each singularity), we have an excision boundary of topology $\mathcal{S}^2$ which suggests that, at least in the neighborhood of each excision boundary, one can use spherical shells (see Fig. 17). Let R_A and R_B be the outer radii of the outermost spherical shells that surround each excision boundary. And let the coordinate centers of the excision boundaries, as set by our initial data solver, be (x_A, y_A, z_A) and (x_B, y_B, z_B). Assume for the simplicity of the discussion that $x_A > x_B$ and $|x_A| \leq |x_B|$. We center the outer shells at the origin of our coordinate system. The inner radius R_C of the outer spherical region is set to approximately three times the distance between the centers of the excision spheres. Next, we need to fill in the space between the outer sphere $\mathcal{S}^3_C[(0, 0, 0), R_C]$ and the two inner spheres $\mathcal{S}^3_A[(x_A, y_A, z_A), R_A]$ and $\mathcal{S}^3_B[(x_B, y_B, z_B), R_B]$.

In order to construct the actual subdomains filling up the space between S^3_A, S^3_B and S^3_C, we will make use of (θ, ϕ) coordinates aligned with the x axis, defined with respect to the centers of either S^3_{EA} or S^3_{EB} (these spheres will be defined below):

$$\phi_A = \tan^{-1}(z/y), \tag{A1}$$

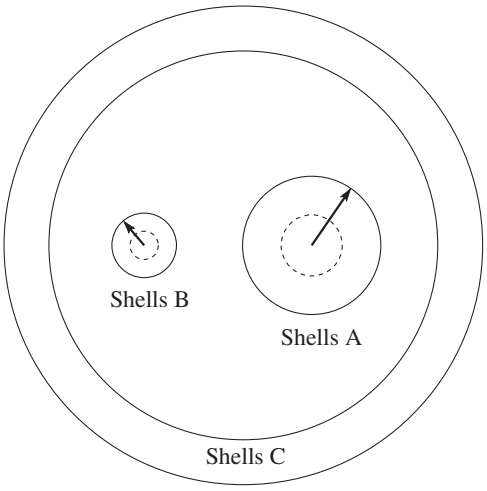

FIG. 17. Schematic geometry of the spherical regions of the grid geometry. The outer radii of the regions around the excision boundaries covered by spherical grid is indicated by arrows. The excision boundaries themselves are marked by circles drawn with dashed line.

$$\theta_A = \cos^{-1}\left(\frac{x - x_{EA}}{\sqrt{(x - x_{EA})^2 + y^2 + z^2}}\right) \tag{A2}$$

with similar definitions for (ϕ_B, θ_B).

We next define a *projection map* used to connect various surfaces with spheres (see Fig. 18). Let $\mathcal{S}_L$ be a surface parametrized by (θ, ϕ). Let $\mathcal{S}^3_U$ be a sphere, and let P_W be a point in the interior of the sphere but not on the surface, $P_W \notin \mathcal{S}_L$.

For each point $Q_L(x^i_L) \in \mathcal{S}_L$, we construct a line connecting Q_L and P_W. This will intersect the sphere in two points. Let $Q_U(x^i_U)$ be the intersection point that is on the same side of P_W as Q_L. Thus, we have defined a rule that associates a unique point $Q_U \in \mathcal{S}^3_U$ to each point $Q_L \in \mathcal{S}_L$. We will label the point Q_U by the same parameters (θ, ϕ) as the associated point Q_L. The projection map is defined as

$$\mathcal{M}(P_W, \mathcal{S}^3_U) := (\rho, \theta, \phi) \rightarrow \frac{1 - \rho}{2} x^i_L(\theta, \phi) + \frac{1 + \rho}{2} x^i_U(\theta, \phi), \tag{A3}$$

where we used ρ as a radial parameter, with range $\rho \in [-1, 1]$. We have

$$\mathcal{M}(-1, \theta, \phi) = x^i_L(\theta, \phi), \tag{A4}$$

$$\mathcal{M}(+1, \theta, \phi) = x^i_U(\theta, \phi). \tag{A5}$$

We associate one projection map with each of the three spheres:

$$\mathcal{M}_C := \mathcal{M}((x_C, 0, 0), \mathcal{S}^3_C), \tag{A6}$$

$$\mathcal{M}_A := \mathcal{M}(x^i_A, \mathcal{S}^3_A), \tag{A7}$$

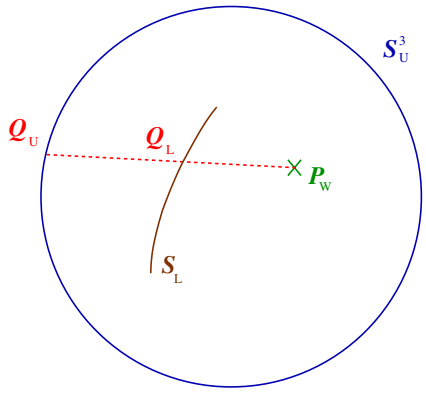

FIG. 18 (color online). Schematic diagram of the projection map used to connect various surfaces with spheres. Given a surface $\mathcal{S}_L$, a point P_W, and a sphere $\mathcal{S}^3_U$, the projection Q_U of a point $Q_L \in \mathcal{S}_L$ is defined by the intersection of the line crossing P_W, Q_L and the sphere $\mathcal{S}^3_U$, such that Q_L is between P_W and Q_U.

$$\mathcal{M}_B := \mathcal{M}(x^i_B, \mathcal{S}^3_B), \tag{A8}$$

where x_C is defined in Eq. (A9). As pointed out in Sec. II B, $x^i_{A/B}$ are slightly offset from the x axis along the y direction.

Next, we divide the volume in the interior of $\mathcal{S}^3_C$, outside of $\mathcal{S}^3_A$ and $\mathcal{S}^3_B$ into wedges of various shapes. First, we pick an $x =$ const plane, $\mathcal{P}_C$ (see Fig. 19), which separates the regions around the two excision boundaries, using

$$x_C = \eta(1-\xi)x_A + \eta\xi x_B, \quad \text{with} \tag{A9}$$

$$\xi = \max\left(\frac{1}{4}, \frac{|x_A|}{|x_A| + |x_B|}\right). \tag{A10}$$

Our preferred value for η is 0.99.

When $\xi \le 1/3$ (corresponding to mass ratios $q \lesssim 2$), we start by constructing a sphere $\mathcal{S}^3_{\rm EA}[(x_{\rm EA}, 0, 0), R_{\rm EA}]$ with

$$x_{\rm EA} = 0.9\eta x_A \tag{A11}$$

$$R_{\rm EA} = \sqrt{(x_{EA} - x_C)^2 + (\eta x_A - x_C)^2}. \tag{A12}$$

The sphere $\mathcal{S}^3_{\rm EA}$ intersects the plane $\mathcal{P}_C$ in a circle

$$\mathcal{S}^2_{\rm ME} := \mathcal{S}^3_{\rm EA} \cap \mathcal{P}_C \tag{A13}$$

with radius

$$r_{\rm ME} = |\eta x_A - x_C|. \tag{A14}$$

On the other side of $\mathcal{P}_C$, we define two concentric spheres (see Fig 19): $\mathcal{S}^3_{\rm EB}[(x_{\rm EB}, 0, 0), R_{\rm EB}]$ and $\mathcal{S}^3_{\rm EE}[(x_{\rm EB}, 0, 0), R_{\rm EE}]$ with

$$x_{\rm EB} = \eta x_B, \tag{A15}$$

$$r_{\rm MB} = r_{\rm ME} \times \max\left(0.4, \left|\frac{\eta x_B - x_C}{\eta x_A - x_C}\right|\right), \tag{A16}$$

$$R_{\rm EE} = \sqrt{(x_{\rm EB} - x_C)^2 + r^2_{\rm ME}}, \tag{A17}$$

$$R_{\rm EB} = \sqrt{(x_{\rm EB} - x_C)^2 + r^2_{\rm MB}}. \tag{A18}$$

These choices imply that $\mathcal{S}^3_{\rm EB}$ intersects $\mathcal{P}_C$ in a circle with radius $r_{\rm MB}$

$$\mathcal{S}^2_{\rm MB} := \mathcal{S}^3_{\rm EB} \cap \mathcal{P}_C. \tag{A19}$$

Next, we define wedges/cylinders filling up the space between the three spherical surfaces, cf. Fig. 20. (In our terminology, *wedges* have topology $I^1 \times B^2$, and *cylinders* have topology $I^1 \times S^1 \times I^1$.)

(i) We connect the $x \ge x_C + (3/2)(x_{\rm EA} - x_C)$ portion of $\mathcal{S}^3_{\rm EA}$ with $\mathcal{S}^3_C$ using $\mathcal{M}_C$ and call this the *CA wedge*.

(ii) We connect the same portion of $\mathcal{S}^3_{\rm EA}$ with $\mathcal{S}^3_A$ using $\mathcal{M}_A$ and call this the *EA wedge*.

(iii) We connect the $x_C \le x \le x_C + (3/2)(x_{\rm EA} - x_C)$ portion of $\mathcal{S}^3_{\rm EA}$ with $\mathcal{S}^3_C$ using $\mathcal{M}_C$ and call this the *CA cylinder*.

(iv) We connect the same portion of $\mathcal{S}^3_{\rm EA}$ with $\mathcal{S}^3_A$ using $\mathcal{M}_A$ and call this the *EA cylinder*.

(v) We connect the points $x^i \in \mathcal{P}_C$ inside $\mathcal{S}^2_{\rm ME}$ but outside $\mathcal{S}^2_{\rm MB}$ with $\mathcal{S}^3_A$ using $\mathcal{M}_A$ and call this the *ME cylinder*.

(vi) We connect the points $x^i \in \mathcal{P}_C$ inside $\mathcal{S}^2_{\rm MB}$ with $\mathcal{S}^3_A$ using $\mathcal{M}_A$ and call this the *MA wedge*.

(vii) We connect the same set of points with $\mathcal{S}^3_B$ using $\mathcal{M}_B$ and call this the *MB wedge*.

(viii) We connect the $x \le x_C - (3/2)|x_{\rm EB} - x_C|$ portion of $\mathcal{S}^3_{\rm EB}$ with $\mathcal{S}^3_C$ using $\mathcal{M}_C$. The portion inside

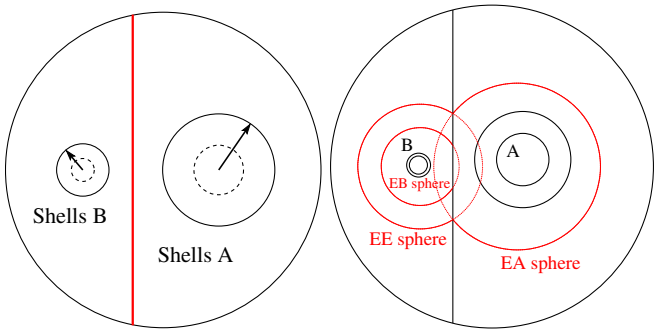

FIG. 19 (color online). Left: Schematic diagram indicating the $x =$ const plane separating the regions around the two excision boundaries. Right: Schematic diagram of the spheres $\mathcal{S}^3_{EA}$, $\mathcal{S}^3_{EE}$, $\mathcal{S}^3_{EB}$.

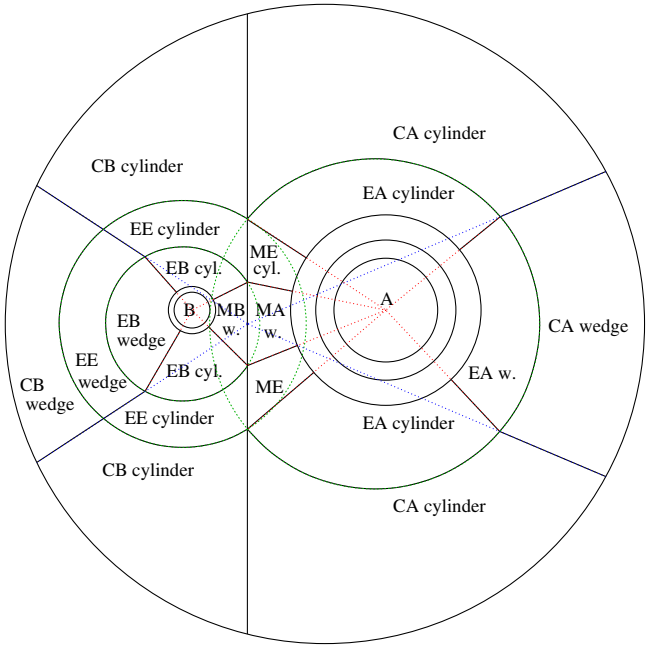

FIG. 20 (color online). Schematic geometry of the touching grid geometry. In a typical simulation, we surround the shown grid geometry by about 20 further spherical shells on the outside, which are not shown in this diagram.

$\mathcal{S}^3_{\rm EE}$ is the *EE wedge*, and the portion between $\mathcal{S}^3_{\rm EE}$ and $\mathcal{S}^3_C$ is the *CB wedge*.

(ix) We connect the same portion of $\mathcal{S}^3_{\rm EB}$ with $\mathcal{S}^3_B$ using $\mathcal{M}_B$ and call this the *EB wedge*.

(x) We connect the $x_C \geq x \geq x_C - (3/2)|x_{\rm EB} - x_C|$ portion of $\mathcal{S}^3_{\rm EB}$ with $\mathcal{S}^3_C$ using $\mathcal{M}_C$. The portion inside $\mathcal{S}^3_{\rm EE}$ is the *EE cylinder*, and the portion between $\mathcal{S}^3_{\rm EE}$ and $\mathcal{S}^3_C$ is the *CB cylinder*.

(xi) We connect the same portion of $\mathcal{S}^3_{\rm EB}$ with $\mathcal{S}^3_B$ using $\mathcal{M}_B$ and call this the *EB cylinder*.

In the cases where $\xi > 1/3$ (corresponding to mass ratios $q \gtrsim 2$), we use a slightly simpler algorithm: we start by constructing $\mathcal{S}^3_{\rm EB}[(x_{\rm EB}, 0, 0), R_{\rm EB}]$ with

$$x_{\rm EB} = \eta x_B, \tag{A20}$$

$$R_{\rm EB} = \sqrt{2} \times |x_{\rm EB} - x_C|. \tag{A21}$$

The sphere $\mathcal{S}^3_{\rm EB}$ intersects $\mathcal{P}_C$ in a circle

$$\mathcal{S}^2_{\rm MB} := \mathcal{S}^3_{\rm EB} \cap \mathcal{P}_C \tag{A22}$$

with radius

$$r_{\rm MB} = |\eta x_B - x_C|. \tag{A23}$$

On the other side of $\mathcal{P}_C$, we define

$$x_{\rm EA} = \eta x_A, \tag{A24}$$

$$R_{\rm EA} = \sqrt{(x_E A - x_C)^2 + r^2_{\rm MB}}. \tag{A25}$$

Once again, $\mathcal{S}^3_{\rm EA}[(x_{EA}, 0, 0), R_{\rm EA}]$ intersects $\mathcal{P}_C$ in a circle

$$\mathcal{S}^2_{\rm MB} := \mathcal{S}^3_{\rm EA} \cap \mathcal{P}_C. \tag{A26}$$

The definition of the various wedges and cylinders in this case is similar to what is used for $\xi \leq 1/3$ with the exception that there are no *EE* or *ME cylinders/wedges*, as $\mathcal{S}^3_{\rm EA} \cap \mathcal{P}_C = \mathcal{S}^3_{\rm EB} \cap \mathcal{P}_C = \mathcal{S}^2_{\rm MB}$.

See Fig. 3 for a 3D snapshot of a grid used for a run with mass ratio 2. This simulation uses the more complicated domain decomposition, although it is close to the dividing line $\xi = 1/3$ where we switch to the simpler domain decomposition. As a last remark, in the runs described here, we have subdivided each wedge (of topology $I^1 \times B^2$) into five distorted cubes.

[1] F. Pretorius, Phys. Rev. Lett. **95**, 121101 (2005).
[2] B. C. Barish and R. Weiss, Phys. Today **52**, 44 (1999).
[3] D. Sigg, and the LIGO Scientific Collaboration, Classical Quantum Gravity **25**, 114041 (2008).
[4] F. Acernese *et al.*, Classical Quantum Gravity **25**, 184001 (2008).
[5] K. Kuroda, and the LCGT Collaboration, Classical Quantum Gravity **27**, 084004 (2010).
[6] K. Somiya, and the KAGRA Collaboration), Classical Quantum Gravity **29**, 124007 (2012).
[7] L. Cadonati *et al.*, Classical Quantum Gravity **26**, 114008 (2009).
[8] B. Aylott *et al.*, Classical Quantum Gravity **26**, 165008 (2009).
[9] P. Ajith *et al.*, Classical Quantum Gravity **29**, 124001 (2012).
[10] The Numerical Relativity and Analytical Relativity (NRAR) Collaboration, https://www.ninja-project.org/doku.php?id=nrar:home.
[11] P. Anninos and S. Brandt, Phys. Rev. Lett. **81**, 508 (1998).
[12] O. M. Moreschi, Phys. Rev. D **59**, 084018 (1999).
[13] J. G. Baker, J. Centrella, D.-I. Choi, M. Koppitz, J. R. van Meter, and M. C. Miller, Astrophys. J. **653**, L93 (2006).
[14] J. A. González, U. Sperhake, B. Brügmann, M. Hannam, and S. Husa, Phys. Rev. Lett. **98**, 091101 (2007).
[15] L. Boyle and M. Kesden, Phys. Rev. D **78**, 024017 (2008).
[16] J. G. Baker, W. D. Boggs, J. Centrella, B. J. Kelly, S. T. McWilliams, and J. R. van Meter, Phys. Rev. D **78**, 044046 (2008).
[17] A. Buonanno, Y. Pan, J. G. Baker, J. Centrella, B. J. Kelly, S. T. McWilliams, and J. R. van Meter, Phys. Rev. D **76**, 104049 (2007).
[18] P. Ajith *et al.*, Phys. Rev. D **77**, 104017 (2008).
[19] L. Santamaría, F. Ohme, P. Ajith, B. Brügmann, N. Dorband, M. Hannam, S. Husa, P. Mösta, D. Pollney, C. Reisswig, E. L. Robinson, J. Seiler, and B. Krishnan, Phys. Rev. D **82**, 064016 (2010).
[20] S. T. McWilliams, B. J. Kelly, and J. G. Baker, Phys. Rev. D **82**, 024014 (2010).
[21] M. Hannam, S. Husa, F. Ohme, D. Müller, and B. Brügmann, Phys. Rev. D **82**, 124008 (2010).
[22] S. T. McWilliams, J. I. Thorpe, J. G. Baker, and B. J. Kelly, Phys. Rev. D **81**, 064014 (2010).
[23] T. Damour and A. Nagar, Phys. Rev. D **77**, 024043 (2008).
[24] T. Damour, A. Nagar, M. Hannam, S. Husa, and B. Bruegmann, Phys. Rev. D **78**, 044039 (2008).
[25] A. Buonanno, Y. Pan, H. P. Pfeiffer, M. A. Scheel, L. T. Buchman, and L. E. Kidder, Phys. Rev. D **79**, 124028 (2009).
[26] Y. Pan, A. Buonanno, M. Boyle, L. T. Buchman, L. E. Kidder, H. P. Pfeiffer, and M. A. Scheel, Phys. Rev. D **84**, 124052 (2011).
[27] E. Berti, V. Cardoso, J. A. Gonzalez, U. Sperhake, M. Hannam, S. Husa, and B. Brügmann, Phys. Rev. D **76**, 064034 (2007).
[28] J. D. Schnittman, A. Buonanno, J. R. van Meter, J. G. Baker, W. D. Boggs, J. Centrella, B. J. Kelly, and S. T. McWilliams, Phys. Rev. D **77**, 044031 (2008).
[29] A. H. Mroué, H. P. Pfeiffer, L. E. Kidder, and S. A. Teukolsky, Phys. Rev. D **82**, 124016 (2010).
[30] A. L. Tiec, A. H. Mroué, L. Barack, A. Buonanno, H. P. Pfeiffer, N. Sago, and A. Taracchini, Phys. Rev. Lett. **107**, 141101 (2011).

[31] J. A. Gonzalez, U. Sperhake, and B. Brügmann, Phys. Rev. D **79**, 124006 (2009).
[32] U. Sperhake, V. Cardoso, C. D. Ott, E. Schnetter, and H. Witek, Phys. Rev. D **84**, 084038 (2011).
[33] H. Nakano, Y. Zlochower, C. O. Lousto, and M. Campanelli, Phys. Rev. D **84**, 124006 (2011).
[34] C. O. Lousto and Y. Zlochower, Phys. Rev. Lett. **106**, 041101 (2011).
[35] M. Hannam, S. Husa, F. Ohme, and P. Ajith, Phys. Rev. D **82**, 124052 (2010).
[36] T. Damour, A. Nagar, and M. Trias, Phys. Rev. D **83**, 024006 (2011).
[37] I. MacDonald, S. Nissanke, and H. P. Pfeiffer, Classical Quantum Gravity **28**, 134002 (2011).
[38] F. Ohme, M. Hannam, and S. Husa, Phys. Rev. D **84**, 064029 (2011).
[39] M. Boyle, Phys. Rev. D **84**, 064013 (2011).
[40] G. Lovelace, M. Boyle, M. A. Scheel, and B. Szilágyi, Classical Quantum Gravity **29**, 045003 (2012).
[41] L. Blanchet, Living Rev. Relativity **9**, 4 (2006), http://www.livingreviews.org/lrr-2006-4.
[42] M. A. Scheel, M. Boyle, T. Chu, L. E. Kidder, K. D. Matthews, and H. P. Pfeiffer, Phys. Rev. D **79**, 024003 (2009).
[43] T. Chu, H. P. Pfeiffer, and M. A. Scheel, Phys. Rev. D **80**, 124051 (2009).
[44] G. Lovelace, M. Scheel, and B. Szilagyi, Phys. Rev. D **83**, 024010 (2011).
[45] http://www.black-holes.org/SpEC.html.
[46] M. Caudill, G. B. Cook, J. D. Grigsby, and H. P. Pfeiffer, Phys. Rev. D **74**, 064011 (2006).
[47] G. B. Cook and H. P. Pfeiffer, Phys. Rev. D **70**, 104016 (2004).
[48] M. A. Scheel, H. P. Pfeiffer, L. Lindblom, L. E. Kidder, O. Rinne, and S. A. Teukolsky, Phys. Rev. D **74**, 104006 (2006).
[49] B. Szilagyi, L. Lindblom, and M. A. Scheel, Phys. Rev. D **80**, 124010 (2009).
[50] A. Buonanno, L. E. Kidder, A. H. Mroué, H. P. Pfeiffer, and A. Taracchini, Phys. Rev. D **83**, 104034 (2011).
[51] H. P. Pfeiffer, D. A. Brown, L. E. Kidder, L. Lindblom, G. Lovelace, and M. A. Scheel, Classical Quantum Gravity **24**, S59 (2007).
[52] M. Boyle, D. A. Brown, L. E. Kidder, A. H. Mroué, H. P. Pfeiffer, M. A. Scheel, G. B. Cook, and S. A. Teukolsky, Phys. Rev. D **76**, 124038 (2007).
[53] G. B. Cook, Phys. Rev. D **65**, 084003 (2002).
[54] J. W. York, Phys. Rev. Lett. **82**, 1350 (1999).
[55] H. P. Pfeiffer and J. W. York, Phys. Rev. D **67**, 044022 (2003).
[56] H. P. Pfeiffer, L. E. Kidder, M. A. Scheel, and S. A. Teukolsky, Comput. Phys. Commun. **152**, 253 (2003).
[57] W. H. Press, S. A. Teukolsky, W. T. Vetterling, and B. P. Flannery, *Numerical Recipes: The Art of Scientific Computing* (Cambridge University Press, New York, 2007), 3rd ed..
[58] L. Lindblom, M. A. Scheel, L. E. Kidder, R. Owen, and O. Rinne, Classical Quantum Gravity **23**, S447 (2006).
[59] H. Friedrich, Commun. Math. Phys. **100**, 525 (1985).
[60] D. Garfinkle, Phys. Rev. D **65**, 044029 (2002).
[61] F. Pretorius, Classical Quantum Gravity **22**, 425 (2005).
[62] C. Gundlach, J. M. Martin-Garcia, G. Calabrese, and I. Hinder, Classical Quantum Gravity **22**, 3767 (2005).
[63] O. Rinne, Classical Quantum Gravity **23**, 6275 (2006).
[64] O. Rinne, L. Lindblom, and M. A. Scheel, Classical Quantum Gravity **24**, 4053 (2007).
[65] J. M. Stewart, Classical Quantum Gravity **15**, 2865 (1998).
[66] H. Friedrich and G. Nagy, Commun. Math. Phys. **201**, 619 (1999).
[67] J. M. Bardeen and L. T. Buchman, Phys. Rev. D **65**, 064037 (2002).
[68] B. Szilágyi, B. Schmidt, and J. Winicour, Phys. Rev. D **65**, 064015 (2002).
[69] G. Calabrese, J. Pullin, O. Reula, O. Sarbach, and M. Tiglio, Commun. Math. Phys. **240**, 377 (2003).
[70] B. Szilágyi and J. Winicour, Phys. Rev. D **68**, 041501(R) (2003).
[71] L. E. Kidder, L. Lindblom, M. A. Scheel, L. T. Buchman, and H. P. Pfeiffer, Phys. Rev. D **71**, 064020 (2005).
[72] L. T. Buchman and O. C. A. Sarbach, Classical Quantum Gravity **23**, 6709 (2006).
[73] L. T. Buchman and O. C. A. Sarbach, Classical Quantum Gravity **24**, S307 (2007).
[74] D. Gottlieb and J. S. Hesthaven, J. Comput. Appl. Math. **128**, 83 (2001).
[75] J. S. Hesthaven, Applied Numerical Mathematics **33**, 23 (2000).
[76] F. Pretorius, Classical Quantum Gravity **23**, S529 (2006).
[77] M. Holst, L. Lindblom, R. Owen, H. P. Pfeiffer, M. A. Scheel, and L. E. Kidder, Phys. Rev. D **70**, 084017 (2004).
[78] L. Lindblom and B. Szilágyi, Phys. Rev. D **80**, 084019 (2009).
[79] M. W. Choptuik and F. Pretorius, Phys. Rev. Lett. **104**, 111101 (2010).
[80] C. Gundlach, Phys. Rev. D **57**, 863 (1998).
[81] G. Lovelace, R. Owen, H. P. Pfeiffer, and T. Chu, Phys. Rev. D **78**, 084017 (2008).
[82] J. D. Brown and J. W. York, Phys. Rev. D **47**, 1407 (1993).
[83] A. Ashtekar and B. Krishnan, Living Rev. Relativity **7**, 10 (2004), http://www.livingreviews.org/lrr-2004-10.
[84] R. Owen, Ph.D. thesis, California Institute of Technology, 2007.
[85] O. Dreyer, B. Krishnan, D. Shoemaker, and E. Schnetter, Phys. Rev. D **67**, 024018 (2003).
[86] G. B. Cook and B. F. Whiting, Phys. Rev. D **76**, 041501(R) (2007).
[87] T. Regge and J. A. Wheeler, Phys. Rev. **108**, 1063 (1957).
[88] F. J. Zerilli, Phys. Rev. Lett. **24**, 737 (1970).
[89] O. Sarbach and M. Tiglio, Phys. Rev. D **64**, 084016 (2001).
[90] O. Rinne, L. T. Buchman, M. A. Scheel, and H. P. Pfeiffer, Classical Quantum Gravity **26**, 075009 (2009).
[91] M. Boyle and A. H. Mroué, Phys. Rev. D **80**, 124045 (2009).
[92] R. A. Matzner, M. F. Huq, and D. Shoemaker, Phys. Rev. D **59**, 024015 (1998).
[93] H. P. Pfeiffer, Ph.D. thesis, Cornell University, 2003.
[94] M. Boyle, L. Lindblom, H. P. Pfeiffer, M. A. Scheel, and L. E. Kidder, Phys. Rev. D **75**, 024006 (2007).
[95] K. Alvi, Phys. Rev. D **64**, 104020 (2001).

[96] M. Boyle, A. Buonanno, L. E. Kidder, A. H. Mroué, Y. Pan, H. P. Pfeiffer, and M. A. Scheel, Phys. Rev. D **78**, 104020 (2008).
[97] M. Ruiz, R. Takahashi, M. Alcubierre, and D. Núñez, Gen. Relativ. Gravit. **40**, 1705 (2008).
[98] L. Blanchet, M. S. S. Qusailah, and C. M. Will, Astrophys. J. **635**, 508 (2005).
[99] E. Berti, V. Cardoso, J. A. Gonzalez, U. Sperhake, M. Hannam, S. Husa, and B. Brügmann, Phys. Rev. D **76**, 064034 (2007).
[100] W. Tichy and P. Marronetti, Phys. Rev. D **78**, 081501 (2008).
[101] E. Barausse and L. Rezzolla, Astrophys. J. **704**, L40 (2009).
[102] A. Buonanno, L. E. Kidder, and L. Lehner, Phys. Rev. D **77**, 026004 (2008).
[103] J. G. Baker, W. D. Boggs, J. Centrella, B. J. Kelly, S. T. McWilliams, M. C. Miller, and J. R. van Meter, Astrophys. J. **668**, 1140 (2007).
[104] C. Loken, D. Gruner, L. Groer, R. Peltier, N. Bunn, M. Craig, T. Henriques, J. Dempsey, C.-H. Yu, J. Chen, L. J. Dursi, J. Chong, S. Northrup, J. Pinto, N. Knecht, and R. V. Zon, J. Phys. Conf. Ser. **256**, 012026 (2010).